# Hydrophilic and Apolar Hydration in Densely Grafted Cationic Brushes and Counterions with Large Mobilities

Raashiq Ishraaq,[1] Tanmay Sarkar Akash,[1] Arka Bera,[1] and Siddhartha Das[1*]

[1]Department of Mechanical Engineering, University of Maryland, College Park, MD 20742

*Corresponding Author Email: sidd@umd.edu

**TOC**

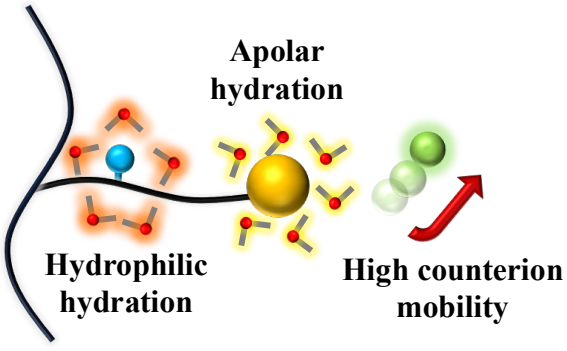

**Abstract**

We employ all-atom MD simulation framework to unravel water microstructure and ion properties for cationic PMETAC or [Poly(2-(methacryloyloxy)ethyl trimethylammonium chloride] brushes with chloride ions as counterions. First, we identify locally separate water regions (with different structural properties) each around the $\{N(CH_3)_3\}^+$ and the C=O functional groups of the PMETAC chain and one around the $Cl^-$ ion. These water regions or domains, which are effectively the first hydration shells around the respective moieties, overlap and the extent of the overlap depends on the nature of the species triggering it. Second, despite the overlap, the water molecules in these domains demonstrate disparate properties dictated by the properties of the atoms/groups around which they are located. For example, the N atom is present as the $\{N(CH_3)_3\}^+$ group in the PMETAC chain and the presence of the methyl groups make the $\{N(CH_3)_3\}^+$ group trigger apolar hydration as evidenced by the corresponding orientation of the dipole of the water molecules within the water domain formed around the $\{N(CH_3)_3\}^+$ moiety. Further, we report that the water molecules constituting the apolar hydration layer around the $N(CH_3)_3\}^+$ group have enhanced tetrahedrality as compared to the water molecules constituting the hydration layer around the C=O group and the $Cl^-$ counterion. Our simulations also identify that there is an intervening water layer between the $Cl^-$ ion and $\{N(CH_3)_3\}^+$ group: the stability of this water layer prevents the $Cl^-$ ion from coming very close to the $\{N(CH_3)_3\}^+$ group, despite the strong electrostatic attraction between these oppositely charged species. As a consequence, there is a significantly large mobility of the $Cl^-$ ions inside the PMETAC brush layer. Furthermore, the C=O group of the PE chain, due to the partial negative charge on the oxygen atom and the specific structure of the system (namely the fact that the C=O group is a part of the PMETAC chains in brush-like configuration and are significantly away from other influencing moieties), demonstrates strongly hydrophilic behavior

and enforces a specific dipole response of water molecules analogous to that experienced by water around anionic species of high charge density. In summary, our findings confirm that PMETAC brushes undergo hydrophilic hydration at one site, apolar hydration at another site, and ensures large mobility of the supported $Cl^-$ counterions.

## INTRDOCUTION

Polymer or polyelectrolyte (PE) chains, when grafted to a solid surface at close-enough proximity to one another, stretch away from the solid surface in the form of brushes.[1-3] These brushes are often responsive to environmental stimuli, such as the pH or the salt concentration of their surrounding solvent. Such responsiveness has been widely leveraged for functionalizing solid surfaces, such as planar surfaces, inner walls of nanochannel or a nanopore, outer surface of nanoparticles, etc., for a vast range of applications such as fabricating smart surfaces,[4] developing biofouling-resistant surfaces,[5] nanofluidic current rectification,[6,7] nanofluidic diode fabrication,[8] ion and biosensing,[9,10] targeted drug and gene delivery,[11,12] oil recovery,[13] water harvesting,[14] and many more. The significance of the problem has prompted extensive research on the topic, with the research methods including theory,[15-20] simulations,[21-30] and experiments.[31-35] In terms of the simulations, the primary approach for studying the polymer and PE brushes has been coarse-grained simulations. Given the fact that the problem primarily focuses on capturing the behavior of long polymer chains and coarse-grained methods are very much adept in simulating large sizes of the polymer chains, coarse grained approaches [21-30] continue to remain the tools of choice for simulating the behavior and properties of polymer and PE brushes.

Very recently, however, there has been a keen interest to probe the behavior of the polymer and PE brushes with a greater degree of granularity. To achieve such a thing, Dormidontova and co-workers studied the behavior of the uncharged PEG (poly-ethylene glycol) polymer brushes using *all-atom molecular dynamics (MD) simulations*.[36-38] These simulations captured the hydration behavior and the tail mobility of PEO brushes for different grafting densities as well as for different substrate curvatures. Other notable studies that have employed all-atom MD simulations for studying the behavior of the uncharged polymer brushes and the brush-supported

water molecules include the papers by Kubo and co-workers,[39] and Yagasaki and co-workers.[40] Very recently, we started to explore in great detail, using all-atom MD simulations, the behavior of *charged polyelectrolyte (PE) brushes* and the brush-supported water molecules and the counterions.[41-49] Our simulations primarily focused on anionic PE brushes, such as PAA [poly(acrylic acid)] or PSS [poly(styrene sulfonate)] brushes and yielded several interesting findings such as identifying water-in-salt electrolyte (WISE) like behavior of the PAA-brush-supported counterions and water molecules,[41,42] the alteration of the hydrogen bonding energetics inside the PE brush layer,[44] the role of multivalent counterions in regulating the counterion bridging effect inside the brush layer,[45] the PE brush charge density dependent changes in the orientation between the PAA and PSS brushes,[46] and coion-driven electrokinetic transport in nanochannels grafted with PAA brushes.[47-49] In this regard, there has been very little work in probing the behavior of *cationic brushes* and such brush-supported water molecules and counterions (anions) using all-atom MD simulations. Very recently, we studied PMETAC brushes using all-atom MD simulations and used machine learning methods to identify the alterations in the characteristics of the water-water hydrogen bonds inside such brush layer.[50] Santos *et al.* also employed all-atom MD simulations for studying the PMETAC brushes: however, their findings primarily focus on the structure, configuration, and hydration of the brushes (with changing salt type) with little analysis of the behavior and properties of the brush-supported water molecules and counterions.[51] Under such circumstances, a detailed understanding of the structure, configuration, and properties of the cationic-brush-supported water molecules and counterions and the role of different atoms of such cationic brushes in dictating these water and ion behaviors, only discernible by the detailed all-atom MD simulations accompanied by deep statistical analysis, remain largely missing.

In this study, we employ all-atom MD simulations to reveal several interesting facets of the PMETAC brush-supported water molecules and counterions. First, the water supported by the PMETAC-brush-$Cl^-$-ion-counterion system is found to form three water domains (or local regions) centered around three entities, namely the N atom [of the $\{N(CH_3)_3\}^+$ moiety] of the PMETAC chain, the C=O group of the PMETAC chain, and the $Cl^-$ ion. These water domains are nothing but the first hydration shells formed around these respective moieties: despite that, we prefer to identify them as "domains" instead of simply referring to them as first hydration shells. This choice stems from the fact that we want to highlight certain specific features that the water molecules in these "domains" or first hydration shells demonstrate. These domains overlap, i.e., the water molecules in one domain are shared by the other domains, and the extent of this overlap depends on the nature of the species triggering these domains. Second, the properties of the water molecules in these domains are dictated by the effects introduced by the different atomic/molecular entities of the PMETAC chains. For example, the N atom is present as the $\{N(CH_3)_3\}^+$ group: due to the presence of the three methyl groups, the $\{N(CH_3)_3\}^+$ group induces apolar hydration. This is supported by the corresponding dipole orientation of the water molecules in the hydration shell (or the water domain) of the $\{N(CH_3)_3\}^+$ group. Furthermore, the tetrahedral order parameter ($q$) of these water molecules in the domain around the $\{N(CH_3)_3\}^+$ group is also greater (i.e., the water molecules in the domain around the $\{N(CH_3)_3\}^+$ group are more structured) as compared to the water molecules in the domain around $Cl^-$ and C=O. Also, there is an intervening water layer between the $\{N(CH_3)_3\}^+$ group and the $Cl^-$ ion and the stability of this layer (primarily attributable to the strongly-bound hydration layer of the $Cl^-$ ion) prevents the $Cl^-$ ion from coming into close vicinity of $\{N(CH_3)_3\}^+$ group despite the strong electrostatic attraction between $Cl^-$ and $\{N(CH_3)_3\}^+$. Accordingly, the $Cl^-$ ions are only weakly attracted to the $\{N(CH_3)_3\}^+$ moieties; as a

result, the $Cl^-$ ions demonstrate significant mobility inside the PMETAC brush layer. Such large mobilities are not witnessed for counterions associated with other types of densely grafted PE brushes, such as poly-acrylic or PAA brushes;[41] however, despite such large mobilities, the $Cl^-$ ions mostly remain confined within the brush layer and do not escape into the bulk. The C=O group of the PMETAC chain, on the other hand, demonstrates strongly hydrophilic behavior: due to the partial negative charges on the oxygen atom and the specific structure of the system, the C=O group enforces the dipole response of water molecules to be similar to that experienced by water around anionic species (e.g., $Cl^-$ ion). Please note that by this "specific structure", we point to the fact that the C=O group is a part of the PMETAC chain in brush-like configuration and the brush configuration is such that the C=O group is significantly away from other influencing entities of the PMETAC chain. Overall, our findings show that despite being a well-known *cationic* PE chain, PMETAC brushes, demonstrate local hydrophilic hydration at one site and apolar hydration at another site and triggers very large mobilities of the $Cl^-$ counterions.

## METHODS

Our all-atom MD simulations considered three separate brush systems with varying grafting density (namely, $\sigma_g$ = 0.15, 0.2 and 0.25 chain/nm$^2$). These grafting density values have been previously considered in experiments.[52-53] Each system consisted of 25 PMETAC chains arranged in a 5 x 5 square array. The PMETAC chains were solvated in water and the water was modeled explicitly using the SPC/E water model.[54] Every PMETAC chain consisted of 24 monomers with methyl capping (see Fig. 1). Such chain length of the PE brushes is sufficient for capturing the structure and properties of the brush-supported water and counterions.[44]

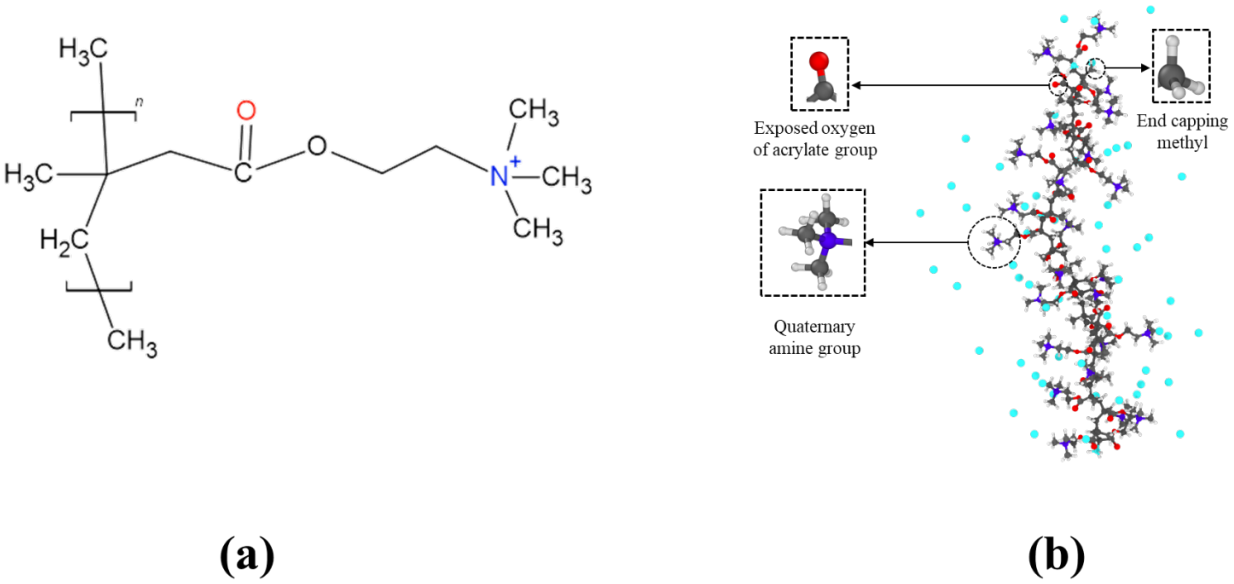


**Figure 1:** (a) Representation of the chemical structure of a single PMETAC monomer (for our simulations, *n*=24). (b) A snapshot of the chain structure. In (b), black, white, blue, red spheres represent the carbon, hydrogen, nitrogen and oxygen respectively.

We carried out all-atom MD simulation using LAMMPS software package.[55] Following our previous papers,[42,44] the initial structure was created as a straight array of chains where columns of counterions were placed adjacent to each chain. We consider an additional added NaCl salt of 0.01 M concentration, with the salt ions ($Na^+$ and $Cl^-$) being placed randomly in the bulk water above the brush layer. The structure was built using Moltemplate.[56] OPLS all-atom forcefield, which is one of the most accurate forcefields for modelling of polymeric systems[57] and has been previously used to model PMETAC brushes[58] (see section S1 in the supporting information for more details), was used to model the interactions between the brush atoms. The water was modeled using the SPC/E model, while for modeling the mobile ions, the parameters from the Joung-Cheatham (J/C) ion model were used.[60] The J/C ion model considers a non-polarizable and spherical force field and the parameter sets were obtained by reproducing the solvation-free energies, radial distribution function, ion-water interaction energies, and lattice constants.[60] Long-range Columbic interactions were calculated using a PPPM (particle-particle particle-mesh) algorithm. The cutoff for the Columbic interactions was chosen as 10.5Å. On the other hand, geometric rules were used in all cases for finding the Lennard Jones (LJ) interaction parameters except for the case of the ion-ion and ion-water LJ interactions (for which the Lorentz-Berthelot mixing rule was used to be consistent with Cheatham *et al.*[60]) Also, the cut-off for the shifted-truncated 12-6 LJ potential was considered as 13 Å.[41] The simulation boundary was considered to be periodic in the x-y direction, while a fixed boundary condition was implemented in the z-direction. LJ walls were maintained at both ends in the z-direction in order to prevent mobile counterion and water from escaping the system.

At first, energy minimization was performed to remove any overlap of atoms. Then the system was run under $NP_zT$ ensemble (where dimensions along the z axis is varied) in order to equilibrate

the pressure at 1 atmospheric pressure. After the pressure equilibration, the result of the simulation was run in an NVT ensemble using a Nosé-Hoover thermostat at 300 K.[36] The equilibration was confirmed by ascertaining that the average brush height fluctuated around a constant value (see Fig. S2 in the SI). After equilibration, the production run was performed for each system for 12 ns. The simulation, the potentials, the system modelling, and the sampling protocols were kept similar to our previous studies.[41,42] The brush height calculation, the brush height autocorrelation function, and all other details of the force fields (including the force field parameters) used in this study have been provided in sections 1 and 2 of the Supporting Information (SI).

## RESULTS

### Configuration of the PMETAC Brushes

Fig. 2(a) shows a snapshot of the brush system, depicting the brushes, water molecules, and the counterions. Fig. 2(b) provides the variation of the brush height as a function of the grafting density. The brush height, as expected, increases with an increase in the grafting density. Fig. 2(c) provides the reduced monomer number density: for all the different grafting density values, the monomer density profiles demonstrate a step-like behavior, which is common for brushes at high grafting densities.[41,61] Finally, Fig. 2(d) shows the endpoint distribution of the brushes: this distribution provides a measure of the flexibility of the chains in the axial direction. An increase in the grafting density leads to a weak increase in the brush height [i.e., the brush height changes from $13\sigma$ to $15\sigma$ as the grafting density increases from 0.15 to 0.25 chains/nm$^2$; please see Fig. 2(b)]. Accordingly, the peak of the end point distribution of the brushes for a greater grafting density shifts slightly to the right [see Fig. 2(d-inset)]. Furthermore, given that for a greater grafting density the number of chains per unit volume is more (i.e., there are a greater number of chains whose end points are counted), the magnitude of the $\rho_e\sigma^3$ peak increases progressively with an increase in the grafting density.

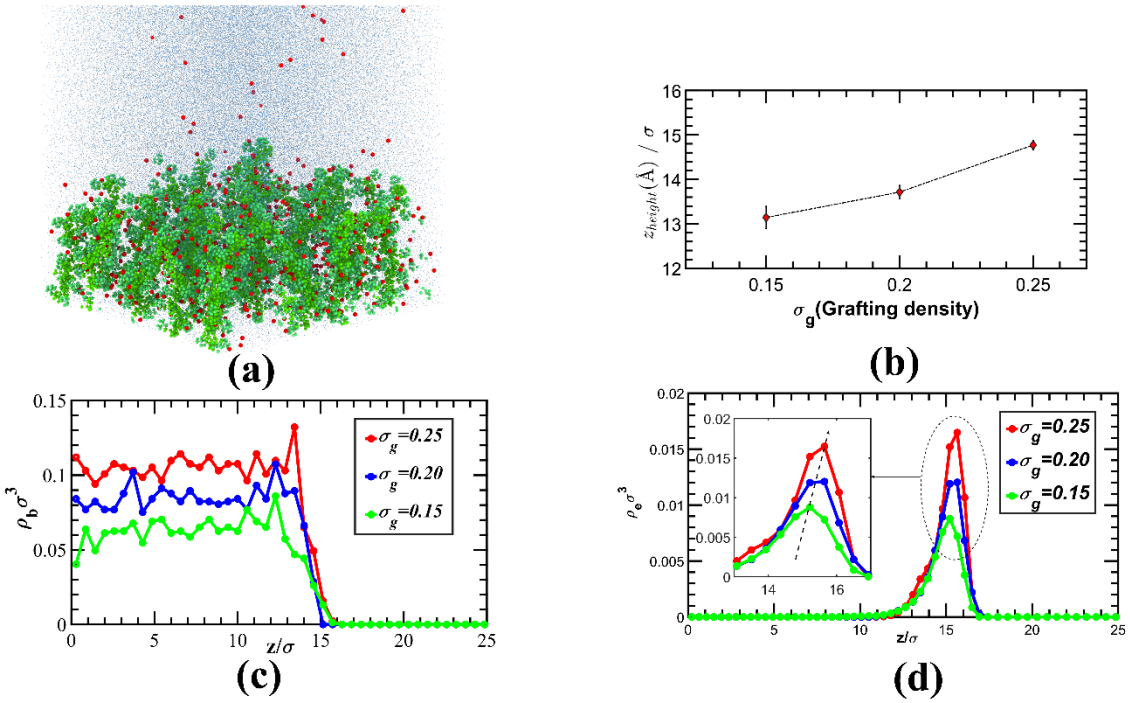


**Figure 2.** (a) MD simulation snapshot (for a grafting density of 0.15 chains/nm$^2$) showing the PMETAC brushes, water molecules, and $Cl^-$ counterions. Green, red and blue (background) respectively represents the brush, counterion and water. (b) Variation of the mean brush height ($z_{height}$) with the grafting density ($\sigma_g$) (see the caption of Fig. S2 in the SI for a detailed procedure employed to calculate the brush height). The unit of the grafting density is in chains/nm$^2$ (c) Profile of the dimensionless monomer density ($\rho_b\sigma^3$), where $\rho_b$ is the monomer density and $\sigma$ is equal to 3.5 Å and the maximum uncertainty ($\Delta\delta_{max}$) among the points reported in the plot is $\pm$ 0.0031 $\rho_b\sigma^3$. (d) Profile of the dimensionless end point density ($\rho_e\sigma^3$) (with the maximum uncertainty among the points reported in the plot being $\Delta\delta_{max}$= $\pm$ 0.0016 $\rho_e\sigma^3$). The dimensionless monomer and endpoint density profiles are measured along the z-axis (normal to the grafting plane). The distance from the plane is also measured in nondimensionalized units (z/σ). In the inset of (d), we magnify the end-point distributions for the $z$ values where the peaks in the distributions occur. The black dotted line (in the inset) shows the trend of the peaks.

**Structure and Properties of the PMETAC-Brush-Supported Water Molecules**

We study the structure and properties of water confined within the PMETAC brush layer. In Fig. 3(a), we show the variation of the average number density of the water molecules with distance from the grafting surface both inside and outside of the PMETAC brush layer. As has been observed for anionic brushes,[41,42] here too, the number density of the water molecules inside the brush layer (i.e., in the space between $z$=5Å to $z$=45Å, measured from the grafting surface) decreases with an increase in the grafting density [see the inset of Fig. 3(a)]. A larger grafting density implies the presence of a greater number of monomers (for a given volume) inside the brush layer, which reduces the available space (for a given volume) for the water molecules inside the brush layer. This leads to the presence of a reduced number of water molecules, leading to a reduced water number density inside the brush layer (i.e., between $z$=5Å to $z$=45Å). Fig. 3(b) confirms this grafting-density-driven reduction in the percentage of atoms belonging to water molecules inside the brush layer (i.e., between $z$=5Å to $z$=45Å). It is useful to note here that several of the main qualitative findings of Figs. 2 and 3, namely a decrease in water number density with an increase in grafting density, an increase in brush height with an increase of grafting density, etc., are common for any densely grafted PE brushes. For example, in our previous papers,[19,41] where all-atom MD simulations were employed to probe the structure and configuration of the anionic PAA (poly-acrylic acid) brushes, we have seen such qualitative results.

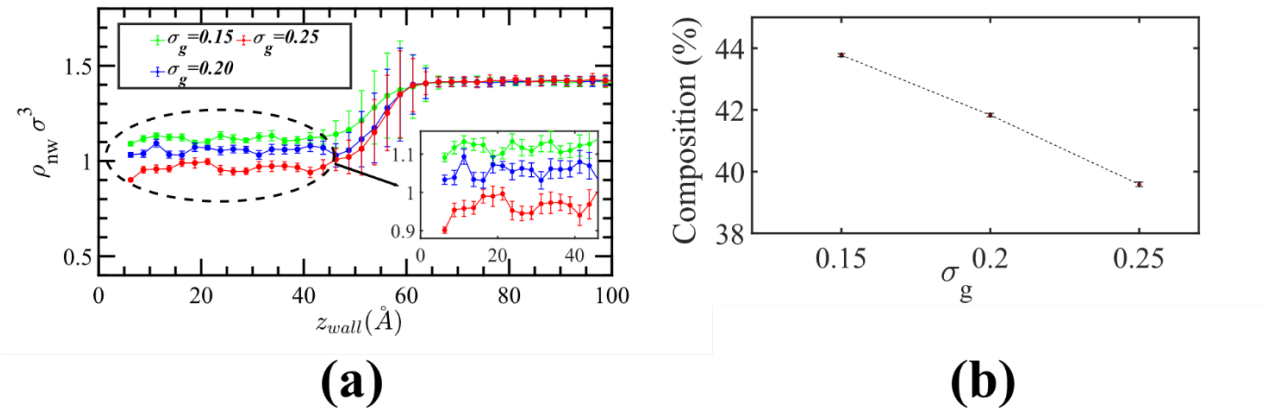


**Figure 3.** (a) Dimensionless density distribution of the water molecules inside and outside the PE brush layer as functions of the PE grafting density ($\sigma_g$). The unit of the grafting density is in chains/nm$^2$. In the inset of (a), we magnify the distribution inside the brush layer (i.e., in the space between $z$=5Å to $z$=45Å, measured from the grafting surface). (b) Grafting-density-driven variation in the percentage of atoms belonging to water molecules inside the brush layer (i.e., in the space between $z$=5Å to $z$=45Å, measured from the grafting surface).

A deeper analysis of the water microstructure inside the brush layer (i.e., between $z$=5Å to $z$=45Å) confirms that there are multiple regions or domains of water molecules inside this PMETAC brush layer in the presence of the $Cl^-$ counterions. These domains are centered around distinct ionic entities of the PMETA-$Cl^-$ system: there is one water domain around the N atom [of the $\{N(CH_3)_3\}^+$ moiety] of the PMETAC brush, another domain around the $O^{\delta-}$ or the oxygen of the C=O group of the PMETAC brush, and the final domain around the $Cl^-$ counterions [see Fig. 4(a)]. These domains are simply the first hydration shells around these different entities. These domains formed around a given entity show significant overlap with each other, and therefore, we like to refer them as "domains" instead of hydration shells. The region identified as the "water domain", in line with the definition of the first solvation shell, is considered as the space between the central atom (X = C, N or Cl) and the first minima of the X-O (X = C, N or Cl; O: Oxygen of the water molecule) RDF. These "water domains" are characterized by the fact that although the water domains around different central atoms (X = C, N or Cl) overlap [see Figs. 4(a,c) and Fig S4 in the Supporting Information], the moieties maintain their specific influence on the water present inside the water domain that are formed around them. As already pointed out, the water domains centered around these separate ionic species are nothing but the 1$^{st}$ solvation shell of these ionic species. This is confirmed by Fig. 4(b): we calculate the solvation number (see section S3.2 of the SI for the calculation procedure) around the N atom [of the $\{N(CH_3)_3\}^+$ moiety], $Cl^-$ ion, and $O^{\delta-}$ atom (of the C=O group). In each case, the solvation number is close to the number predicted by the experiments as well as *ab-initio* simulations.[62-66]

At first, we calculate the extent of overlap of these domains: in other words, we are interested to understand to what extent the water molecules in the domain centered around a given species is shared in the water domain centered around another species. Fig. 4(c) provides a pie chart that

shows the extent to which the water molecules centered around a given species is shared by other species for a grafting density of $\sigma_g$= 0.25 chains/nm$^2$. For other grafting densities, the results remain qualitatively similar (see section S3.2 of the SI for more details). For example, for $\sigma_g$ = 0.25 chains/nm$^2$, for the water molecules in the domain centered around the N atom [of the $\{N(CH_3)_3\}^+$ moiety], 65% of the water molecules are not shared with any other species, 6% is shared with C=O group, 28% is shared with $Cl^-$ ion and 1% is common (shared among all moieties). On the other hand, for the water molecules in the domain centered around the $Cl^-$ ion, the majority (78%) is shared with the $\{N(CH_3)_3\}^+$ group and almost nothing (<1%) is shared with the C=O group, while a small fraction (19%) is retained to itself. Finally, for the water molecules in the domain centered around the C=O group, the majority (79%) is shared with the $\{N(CH_3)_3\}^+$ group and almost nothing (<1%) is shared with the $Cl^-$, while a small fraction (6%) is retained to itself. The C=O group of the PMETAC chain, due to the partial negative charge on the oxygen atom, will remain significantly away from the $Cl^-$ counterion: this explains the very little mutual sharing of the water molecules between these two species.

It is important to note here that even though there is a significant overlap between the water domains (as elucidated above), the different moieties maintain their specific influence on the water molecules in their respective water domains. This influence maintained can be attributed to the specific structure of the PMETAC polyelectrolyte brushes, where (1) the chains, being in the "brush-like" configuration, are stretched in a unidirectional manner and (2) the atoms are separated due to bonds [atoms such as N and O (of C=O)] or due to the presence of the methyl groups (atoms such as Cl and N).

In order to further investigate the microstructure, we plot the N-$O_w$, $Cl^-$-$O_w$, and $O^{\delta-}$-$O_w$ radial distribution functions (RDFs) [see Fig. 4(d)]. Here $O_w$ refers to the oxygen atom of the water

molecule, while $O^{\delta-}$ refers to the oxygen of the C=O group. The magnitude of the RDF peaks around these moieties varies significantly, indicating that the density of water molecules varies significantly inside these domains. The peaks of both the $Cl^-$-$O_w$ and $O^{\delta-}$-$O_w$ RDFs occur at a very small distance, confirming that the water molecules are very close to the $Cl^-$ counterion and the C=O group of the PMETAC chains. Also, the height of the first $O^{\delta-}$-$O_w$ RDF peak is less than unity, indicating that water molecules are less accessible in that region. This phenomenon can be attributed to the fact that the C=O moiety is close to the base of the polymer, resulting in poor hydration of the moiety. On the other hand, the peak of the N-$O_w$ RDF occurs at a much larger distance due to the steric hinderance of the $CH_3$ groups. Moreover, the peak of the N-$O_w$ RDF is much blunter as compared to the peaks of the $Cl^-$-$O_w$ and $O^{\delta-}$-$O_w$ RDFs. This indicates that the water molecules around $\{N(CH_3)_3\}^+$ moiety is not strongly affected by its charge and demonstrate only weak interactions with the $\{N(CH_3)_3\}^+$ group. Such a trend for the RDFs is observed for other grafting densities as well (see section S3.1 of SI). Additionally, we plotted the N-$Cl^-$ RDF (see section S4 of SI) for different grafting densities. In Fig. 4(e), we show that for all grafting densities, the values of the locations of the peaks the N-$O_w$ RDF remains smaller than the values of the N-$Cl^-$ RDF peaks: this indicates that for the $\{N(CH_3)_3\}^+$ group, water molecules are closer than the $Cl^-$ ion. This trend persists even when there is an increase in the grafting density (i.e., there are a greater number $Cl^-$ ions in a given volume around the PMETAC brush). The N-$O_w$ RDF starts to rise at a shorter distance than N-$Cl^-$ RDF (see section S4 of SI), which also indicates that water molecules and not $Cl^-$ ion, is closer to $\{N(CH_3)_3\}^+$ moiety. These information confirm the presence of an intervening water layer between the $\{N(CH_3)_3\}^+$ moiety and $Cl^-$ ion; in other words, for the present case, $\{N(CH_3)_3\}^+$ moiety and $Cl^-$ ion behave as solvent-separated ion pair. The consequence of such intervening water layer (and the fact that this water layer is very stable) is

that the $Cl^-$ ions remain excluded from close vicinity of the $\{N(CH_3)_3\}^+$ moiety despite the obvious electrostatic attraction between $Cl^-$ and $\{N(CH_3)_3\}^+$. In summary, Figs. 4(a-e) confirm the presence of distinct water domains around different entities of the PMETA-$Cl^-$ ion system: these water domains are localized at disparate average distances from these different entities and are also shared by other entities.

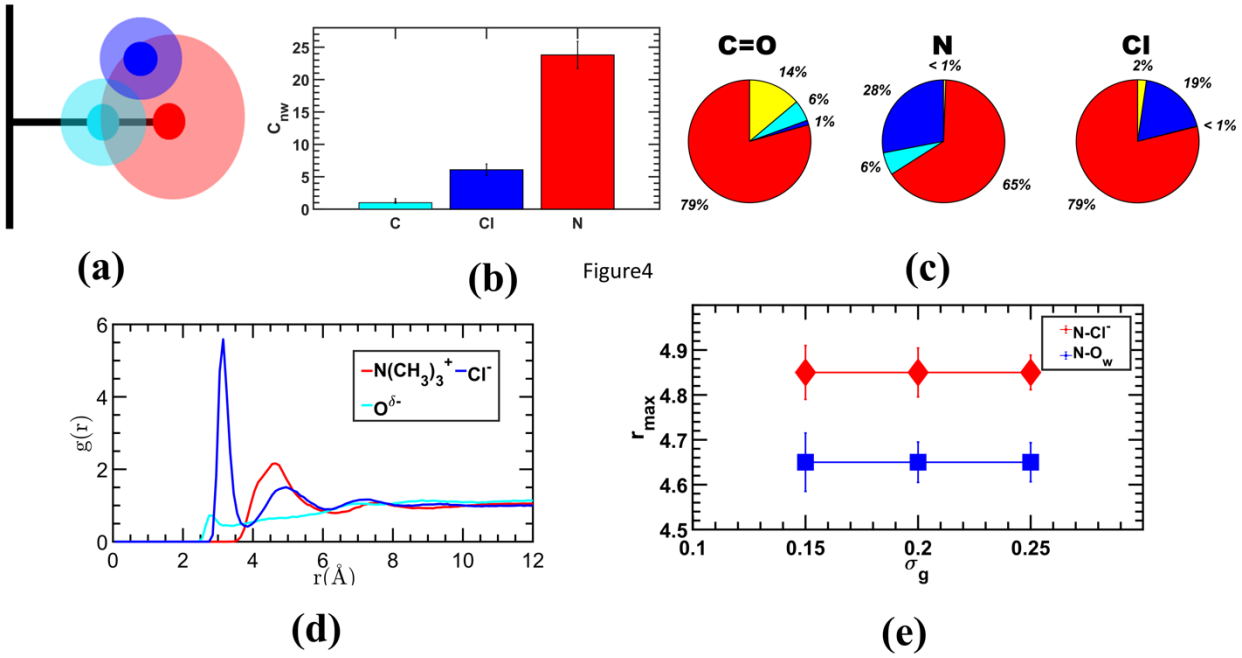


**Figure 4.** (a) Schematic showing the formation of three distinct water domains around the three moieties [N atom (of the $\{N(CH_3)_3\}^+$ moiety) and C=O group of the PMETAC chain] and $Cl^-$ ion. (b) Solvation number around the N atom [of the $\{N(CH_3)_3\}^+$ moiety] and the C=O group of the PMETAC chain and $Cl^-$ ion. (c) Pie charts showing the percentage of the water molecules present in the domains around the C=O (left), N atom [of the $\{N(CH_3)_3\}^+$ moiety] (center), and $Cl^-$ (right) that are shared by other species. Red, blue and cyan respectively represents the % of shared water molecules only with $N(CH_3)_3\}^+$, $Cl^-$ and C=O group. Yellow represents % of water molecules shared with all the moieties. d) N-$O_w$, $Cl^-$-$O_w$, and $O^{\delta-}$-$O_w$ RDFs. (e) Values of the locations of the peaks ($r_{max}$) of the N-$O_w$ and N-$Cl^-$ RDFs plotted as functions of the PMETAC grafting densities.

The water molecules in these distinct domains formed around the different species demonstrate disparate properties. However, it is important to understand how the charge (or partial charge) of each functional group affects the surrounding water molecules in such an environment: a quantification of the dipole orientation of the water molecules in these domains formed around different species enable us to do that. Fig. 5(a) provides the electrical dipole orientation of the water molecules inside these distinct domains. It has been already pointed out above that these water molecules inside these domains are nothing but the water molecules within the 1$^{st}$ solvation shell of the species, namely, the $\{N(CH_3)_3\}^+$ and the C=O groups of the PMETAC chains and the $Cl^-$ counterion. The ideal water dipole orientation around hydrophilic anionic and cationic solutes should be $180^0$ and $0^0$ degrees, respectively [see Fig. 5(b)].[64] Of course, in actual systems, the orientation of the water dipoles deviates from these ideal values on account of the thermal excitation and the energetic penalty associated with the unfavorable positioning (of these water molecules) relative to the adjacent water molecules. On the other hand, depending on the size and the shape of the solute, the dipole orientation of the water molecules around a hydrophobic solute shows a range, but tends to prefer tangential direction for symmetrical entities.[64,67] For our case ($\sigma_g$=0.25 chains/nm$^2$), the water dipoles around $Cl^-$ ion is mostly oriented around $130^0$, which is the typical behavior for water molecules present in the first solvation shell of a hydrophilic anion.[68] It also indicates the water molecules are strongly bound (due to high attraction) to the $Cl^-$ ion and $Cl^-$ ion has a tightly-bound hydration shell. On the other hand, though being cationic, the water dipole orientation around the $\{N(CH_3)_3\}^+$ moiety peaks around $75^0$ indicating that the $\{N(CH_3)_3\}^+$ moiety triggers an apolar-like hydration. This result highlights the manner in which the effect of the charge of the $\{N(CH_3)_3\}^+$ moiety is overwhelmed by the hydrophobic influences of the three methyl ($-CH_3$) groups. Such apolar hydration-inducing tendencies of the $\{N(CH_3)_3\}^+$ entity (of

PMETAC brush) can be surmised from two factors. First, a significant amount of the reported literature indicates the strongly hydrophobic nature of the quaternary amines due to the presence of the hydrophobic methyl groups.[63,65] Second, in our recent machine learning-based analysis of the water structure inside densely grafted PMETAC brushes, it has been revealed that the $H-O'-O$ angle (here "H" is the hydrogen atom, "O" is the donor oxygen atom, and "$O'$"" is the acceptor oxygen atom), characterizing the water-water hydrogen bonding, gets reduced for the water-water hydrogen bonds (HBs) formed inside the PMETAC brush layer as compared to the water-water HBs formed inside the bulk.[50] Such a reduction in the $H-O'-O$ angle implies that the water-water HBs become more linear and hence stronger. This phenomenon also indicates water-water attraction strength increases due to weak $\{N(CH_3)_3\}^+$-water interaction or apolar hydration. On the other hand, the dipole orientation of water molecules within the domain around the C=O group (the C=O demonstrates strongly hydrophilic behavior) of the PMETAC chains is similar to that of water molecules around an anion with high charge density, *i.e.*, very much like that around the $Cl^-$ ion. Such a scenario stems from (1) the presence of the partial negative charges on the O atom of the C=O moiety and (2) the fact that the C=O moiety is a part of the PMETAC chains that are stretched out in a "brush-like" 1D configuration (without any coiling) and that the C=O moiety is somewhat separated from other influencing functional groups of the PMETAC chains (due to the specific structure of the PMETAC chains). *Overall, inside the PMETAC brush layer, there is hydrophilic hydration at one site and apolar hydration at another site.*

It is worthwhile to point out here that the dipole orientation of the water molecules around the $\{N(CH_3)_3\}^+$ moiety is calculated by considering the nitrogen atom as the reference point. We did calculate the same dipole moment of the water molecules around the $\{N(CH_3)_3\}^+$ moiety by considering the hydrogen atoms of the $\{N(CH_3)_3\}^+$ moiety as the reference point. Fig. 5(c)

compares the two cases, i.e., the water dipole moments around the $\{N(CH_3)_3\}^+$ moiety calculated with N and H atoms as reference points: we see very little change in the dipole moment distribution between these two cases. Also, we shall like to point out that the apolar hydration of the $\{N(CH_3)_3\}^+$ moiety stems from the fact that the charges of hydrogen atoms present in the moiety ($0.1e$) is much less than the charges of a water molecule. Therefore, water molecules interacts weakly with the $\{N(CH_3)_3\}^+$ functional group. Also, there are several experimental studies[62,69-71] that have specifically pointed out the apolar hydration of the $\{N(CH_3)_3\}^+$ moiety [or more specifically, the apolar hydration of the $\{N(CH_3)_4\}^+$ ion, i.e., the Tetramethylammonium (TMA) ion].

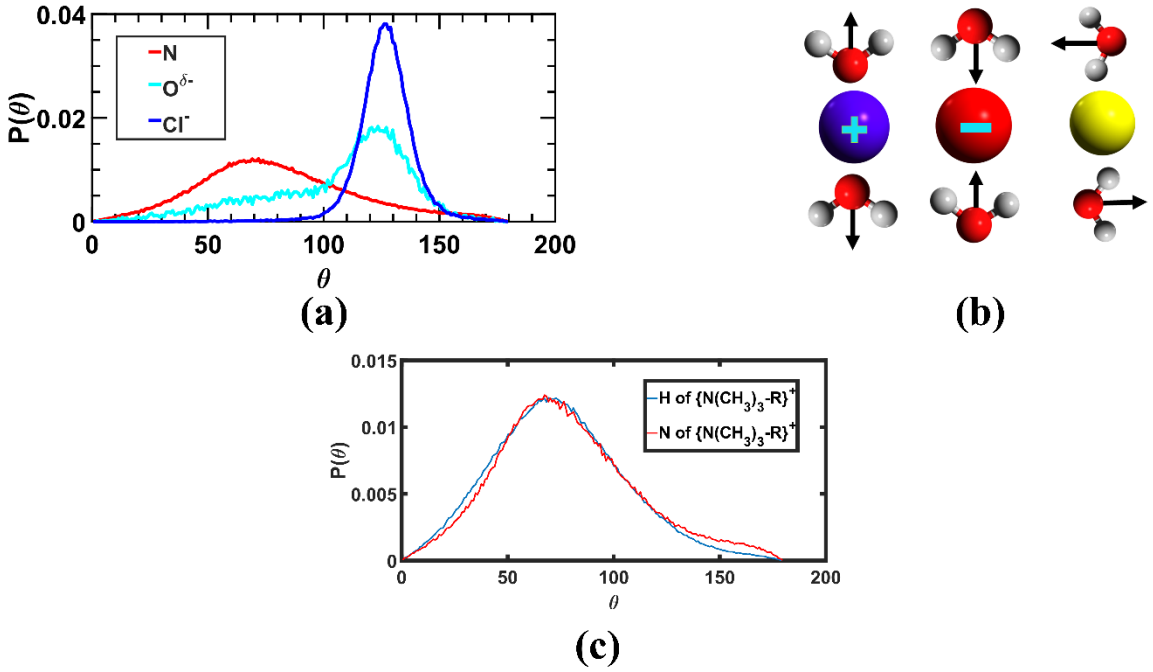


**Figure 5.** (a) Probability distribution of the orientation angle of the water dipole for the water in the three separate domains, namely water around the N atom [of the $\{N(CH_3)_3\}^+$ moiety], C=O group, and $Cl^-$ ion for a grafting density of $\sigma_g$ = 0.25 chains/nm$^2$ (results for $\sigma_g$ = 0.15 chains/nm$^2$ and $\sigma_g$ = 0.2 chains/nm$^2$ have been provided in section S5 of the SI). (b) Schematic showing the orientation of a water molecule around an ideal cation, an ideal anion, and a hydrophobic solute. (c) Comparison of the probability count distribution of dipole orientation of water molecules in the vicinity of the $\{N(CH_3)_3\}^+$ moiety considering the N atom or the H atoms of the $\{N(CH_3)_3\}^+$ moiety as the reference point. The results are for a grafting density of $\sigma_g$ = 0.25 chains/nm$^2$.

Finally, in Fig. 6, we provide the probability count distribution (for $\sigma_g$=0.25 chain/nm$^2$) of the tetrahedral order parameter (given by Errington and Debendetti[72]) of the water molecules in these different domains, or the water molecules associated with the solvation shells of the $\{N(CH_3)_3\}^+$ moiety and the C=O group of the PMETAC chains and the $Cl^-$ counterions. Such tetrahedral order parameter ($q$) gives a measure of the structural order: the greater the value of $q$ more structured are the water molecules (see section S6 of SI for more details). A high tetrahedral order parameter (closer to 1) means the solvating water molecules are in a perfect tetrahedron (like ice); that is the reason for which for a greater value of the order parameter, the water molecules are considered to be "more structured". The water molecules in the solvation shell (or the water domain) of the $\{N(CH_3)_3\}^+$ moiety show a greater value of $q$ as compared to the water molecules in the solvation shell or water domain of the $Cl^-$ counterion or the C=O group. As mentioned before, the charges of hydrogen atoms present in the $\{N(CH_3)_3\}^+$ moiety (0.1$e$) is much lower than water molecules. Therefore, water molecules try to form relatively stronger interactions with other water molecules than the moiety itself, resulting in enhanced $q$ parameter of the water molecules present in the domain around the $\{N(CH_3)_3\}^+$ group. On the other hand, the significantly low tetrahedral order parameter of the hydration shell water around the C=O group, which signifies reduced structuring of water molecules around the C=O group, can be attributed partly to the partial charges of the C=O group and the resulting hydrophilic hydration (such hydration, stemming from the strongly hydrophilic behavior of the C=O group, leads to stronger C=O-water interactions causing a reduced water structural order) and partly to the presence of other methyl groups surrounding the C=O group. The low tetrahedral ordering of the water molecules around the $Cl^-$ atom can be primarily attributed to its high charge density and its resulting interactions with the surrounding water molecules (such interactions distort the water tetrahedron more and consequently the $q$

parameter decreases). We also studied the tetrahedral order parameter of the water molecules around these different entities for other grafting densities ($\sigma_g$=0.20 and 0.15 chains/nm$^2$): the results are provided in the SI and demonstrate similar behavior. Moreover, an increase in the grafting density weakly decreases the tetrahedral order parameter, i.e., reduces the extent of water structuring: this is evident in a small decrease in the fraction of the water molecules with greater $q$ values and a slight leftward shift of the peak in the $P(q)$-*vs*-$q$ distribution [see Fig. 6-inset and Fig. S7 in the SI].

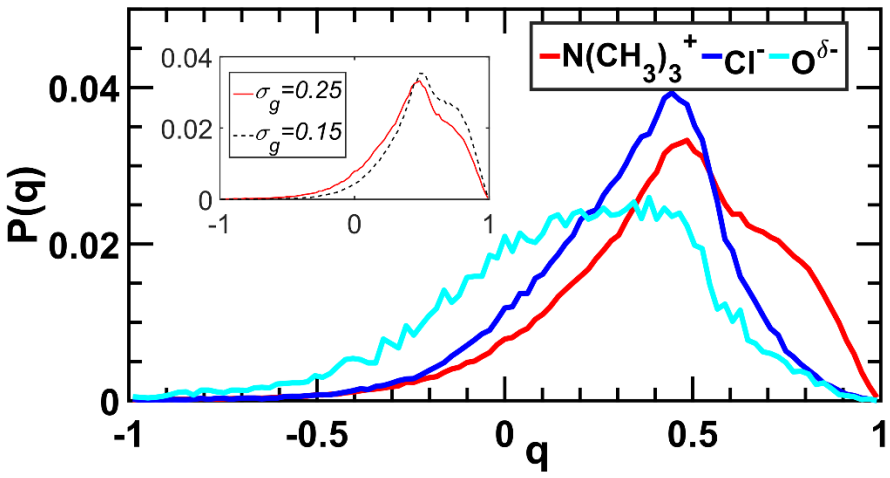


**Figure 6.** Variation of the tetrahedral order parameter for the water in the three separate domains, namely water around $\{N(CH_3)_3\}^+$ group and C=O group of the PMETAC chain and $Cl^-$ ion. These results are all for a grafting density of $\sigma_g$ = 0.25 chains/nm$^2$. (Inset) Comparison in the variation of the tetrahedral order parameter for the water in the domain formed around $\{N(CH_3)_3\}^+$ group between the cases of $\sigma_g$ = 0.25 chains/nm$^2$ and $\sigma_g$ = 0.15 chains/nm$^2$.

**Structure and Properties of the PMETAC-Brush-Supported $Cl^-$ Counterions**

The multiple water domains inside the PMETAC brush layers involve the counterions as well, given the fact that one of the domains is around the $Cl^-$ ion. Therefore, a complete description of the problem must involve a detailed accounting of the counterion properties and behaviors inside the PMETAC brush layer. First, in Fig. 7(a), we plot the dimensionless counterion number density as a function of the grafting density of the PMETAC brushes. An increase in the grafting density will imply a greater number of charged monomers for a given volume; therefore, in order to balance the monomer charges, there will be a larger number of counterions in a given volume. This ensures that the counterion number density increases as a function of the grafting density. On the other hand, in Fig. 3, we have pointed out that the water density *decreases* with an increase in the grafting density. Despite such opposite trends, the relative distances between the $Cl^-$ ion and N atom and the N atom and water molecule remain the same for all values of the grafting density, with N-$O_w$ RDF peak distance being smaller than the N-$Cl^-$ RDF peak distance for all grafting densities [see Fig. 4(e)]. Such trends in the N-$O_w$ and N-$Cl^-$ RDFs with the PMETAC grafting density, despite the grafting density influencing the counterion and water concentrations differently, can be mainly attributed to the stable intervening water layer between $\{N(CH_3)_3\}^+$ and $Cl^-$ that forces the $Cl^-$ ion to remain at large-enough distance from the $\{N(CH_3)_3\}^+$ group despite the electrostatic attraction between the $\{N(CH_3)_3\}^+$ moiety and $Cl^-$ ions.

We next attempt to quantify the mobility of the counterions inside the PMETAC brush layer. For that purpose, we calculated the probability distribution function of the distances traveled by a $Cl^-$ counterion in 40 picoseconds as a function of the PMETAC brush grafting density [see Fig. 7(b)]. We compare this result with the probability distribution function of the distances traveled by a $Na^+$ counterion inside a PAA brush layer. All-atom MD simulation data for the PAA

brush layer that has been used for this figure has been generated from the parameters of our previous study.[42] The grafting density of the PAA brush layer is 1.67 chains/nm$^2$, which tantamounts to a brush-brush separation distance of $l = \sqrt{\frac{1}{1.67/nm^2}} = 7.73$Å. On the other hand, the maximum grafting density considered for the PMETAC chains is 0.25 chains/nm$^2$ that converts to a brush-brush separation distance of $l = \sqrt{\frac{1}{0.25/nm^2}} = 20$Å. However, there are bulky side chains on two sides of the PMETAC chains, ensuring an effective reduction of the brush-brush separation distance for the PMETAC brushes. Interestingly, the number density of the solvating water molecules for these two separate cases, namely the case of PAA brush layer with a grafting density of 1.67 chains/nm$^2$ and the case of the PMETAC brush layer with a grafting density of 0.25 chains/nm$^2$, closely resemble with one another [see Fig. 7(c)]. This implies both these systems, with disparate grafting densities, exert a similar degree of confinement to the solvating water.[46] Accordingly, we can hypothesize that the effective chain-chain separation distance for the PMETAC brushes (for a grafting density of 0.25 chains/nm$^2$), on account of the bulky side chains, will be similar to the chain-chain separation distance of the PAA brushes (for a grafting density of 1.67 chains/nm$^2$). Despite that, we find that the distance traversed by the $Cl^-$ ions inside the PMETAC brush layer (for a grafting density of 0.25 chains/nm$^2$) is several times greater than the distances traversed by the $Na^+$ ions inside the PAA brush layer (for a grafting density of 1.67 chains/nm$^2$) [see Fig. 7(b)]. This confirms the significantly large mobility of the $Cl^-$ counterions inside the PMETAC brush layer and this can be attributed to the weak attraction of the $Cl^-$ ions to the $\{N(CH_3)_3\}^+$ groups of the PMETAC chains owing to the failure of the $Cl^-$ ions to come to close enough proximity of the $\{N(CH_3)_3\}^+$ group, as confirmed by Fig. 4(e). Additionally, we calculated the probability distribution for $\sigma_g$=0.15 and 0.2 chains/nm$^2$ [shown in Fig. 7(d)], which shows a

slight increase in counterion mobility due to the reduction of the steric hindrance at lower grafting densities. Therefore, it can be concluded that the chemical nature of the confining medium plays a greater role on dictating counterion mobility than the degree of confinement (or grafting density). In order to further showcase the enhanced mobilities of the counterions inside the PMETAC layers, we plot the MSD (mean square displacement) of the counterions inside the PMETAC brush (for different grafting densities) and the PAA brush (with a grafting density that enables a similar degree of confinement for the solvating water as the PMETAC brush layer with a grafting density of $\sigma_g$= 0.25 chains/nm$^2$) [see Fig. 7(e)]. This MSD is calculated using eqs.(1) below:

$$MSD(t) = \langle (r(t) - r_0)^2 \rangle . \quad (1)$$

$$D = \frac{1}{6} \lim_{t \to \infty} \frac{d}{dt} \langle (r(t) - r_0)^2 \rangle . \quad (2)$$

In eqs.(1,2), $r(t)$ is the position of the a particle at time t, $r_0$ is the initial position of the particle, and $< >$ denotes the average over all the particles and different initial positions, and $D$ is the diffusion coefficient. The MSD values clearly demonstrate the significantly large mobilities of the counterions inside the PMETAC brush layer (especially for the case of weak grafting density values). For PAA it shows that the $Na^+$ atoms are completely immobilized and are fluctuating in their respective positions. Table 1 shows the diffusion coefficients calculated for all the systems. The diffusion coefficient (D) has been calculated from the Einstein formula by using the slope of the MSD curve [81] (Eq. 2). From the table we can see that the diffusion coefficient for PMETAC brushes with a grafting density of $\sigma_g$= 0.25 chains/nm$^2$ is significantly higher than PAA brushes. Therefore, for a similar degree of confinement, despite $Na^+$ ion having lower mass (23 amu) than $Cl^-$ (35.5 amu), the mobility and diffusivity of the $Na^+$ ions inside PAA-brush-$Na^+$-counterion

system is much less than the mobility and diffusivity of the $Cl^-$ ions inside PMETAC-brush-$Cl^-$-counterion system.

Finally, in Fig. 8, we compare the number density distribution of the N atom [of the $\{N(CH_3)_3\}^+$ groups] and $Cl^-$ ions and observe that there is very little difference between these number densities within the brush layer. Hence, we can infer that most of the $Cl^-$ counterions remain inside the brush layer despite having high mobility. Therefore, we can hypothesize that inside the brush layer, the counterions are not strongly attracted to a fixed oppositely charged site on the brushes, but rather move around inside the brush layer without actually leaving the brush layer.

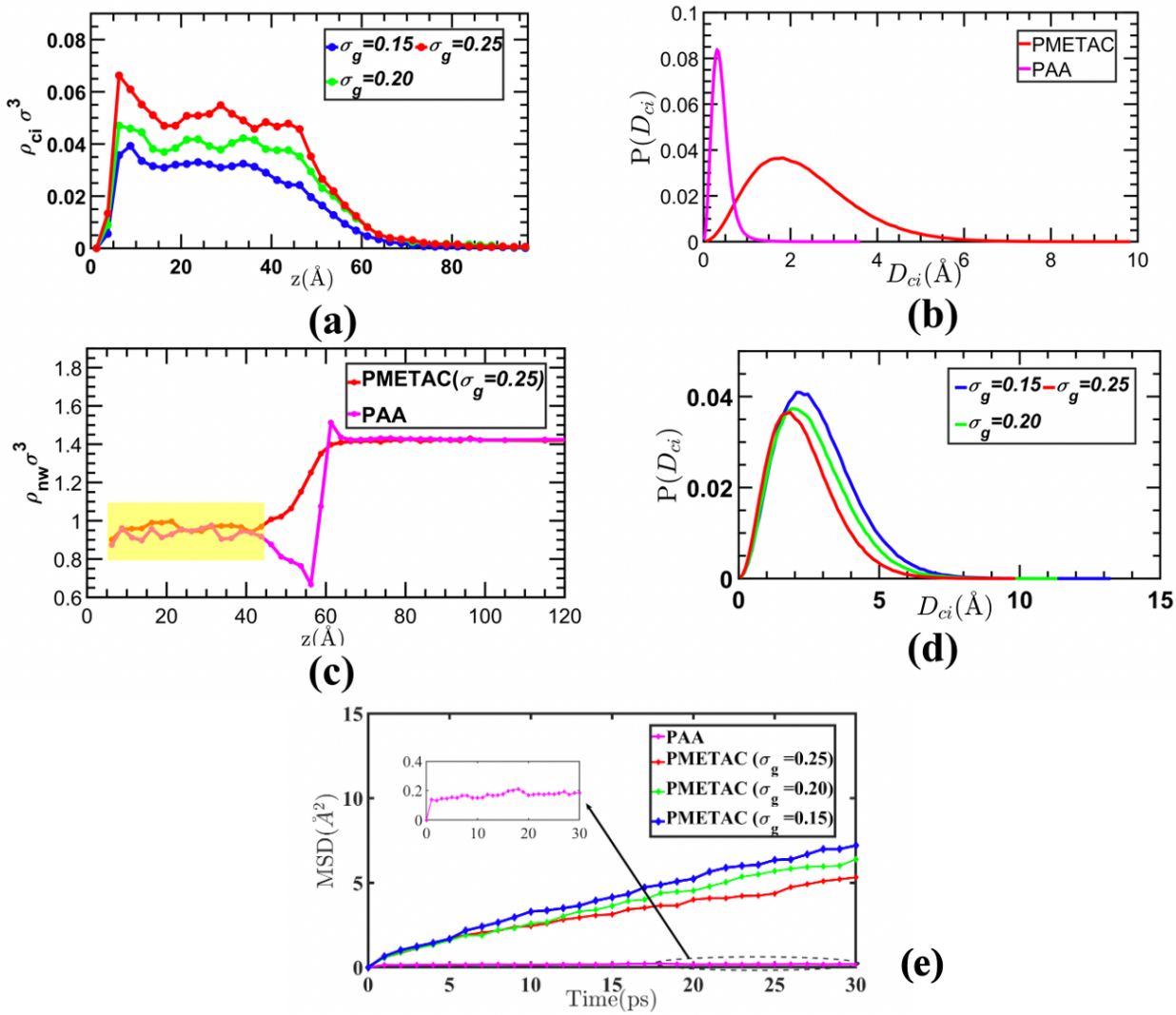


**Figure 7.** (a) Dimensionless density distribution of the $Cl^-$ counterions inside and outside the PMETAC brush layer as functions of the PMETAC brush grafting densities (the maximum uncertainty among the points reported in the plot being $\Delta\delta_{max}$= ± 0.0403 $\rho_{ci}\sigma^3$). (b) Distribution of the average distances traversed by the counterions for PAA and PMETAC. The results (of the PMETAC) are compared with the average distances traversed by a $Na^+$ ion inside the PAA brush layer having $\sigma_g$= 1.67 chains/nm$^2$. (c) Dimensionless water density distribution of PMETAC brush layer ($\sigma_g$= 0.25 chains/nm$^2$) and PAA brush layer ($\sigma_g$= 1.67 chains/nm$^2$) with $Na^+$ counterions (the maximum uncertainty among the points reported in the plot being $\Delta\delta_{max}$= ± 0.136 $\rho_{nw}\sigma^3$). The sampling region (5Å to 45 Å from lower wall) is shaded in yellow. (d) Distribution of the average

distances traversed by the counterions for of PMETAC for different grafting densities ($\sigma_g$= 0.15,0.2 and 0.25 chains/nm$^2$). (e) MSD variation of the counterions inside the PMETAC brush layer (counterions are $Cl^-$ ions) and the PAA brush layer (counterions are $Na^+$ ions). The results are shown for the PMETAC brush layer with three different grafting density values, while for the PAA brush layer the grafting is $\sigma_g$= 1.67 chains/nm$^2$ (i.e., a grafting density that enables a similar degree of confinement for the solvating water as the PMETAC brush layer with a grafting density of $\sigma_g$= 0.25 chains/nm$^2$). In the inset of Fig. 7(e), the MSD plot for the $Na^+$ ions inside the PAA brush layer have been magnified.

**Table 1:** Diffusivities (D) of the $Na^+$ ions inside PAA-brush-$Na^+$-counterion system and the $Cl^-$ ions inside PMETAC-brush-$Cl^-$-counterion system.

| **Counterion** | **D x $10^{-10}$ ($m^2/s$)** |
|---|---|
| $Cl^-$ (inside PMETAC brushes, $\sigma_g = 0.15$ chains/$nm^2$) | 3.61± 0.3626 |
| $Cl^-$ (inside PMETAC brushes, $\sigma_g = 0.20$ chains/$nm^2$) | 3.09 ± 0.3339 |
| $Cl^-$ (inside PMETAC brushes, $\sigma_g = 0.25$ chains/$nm^2$) | 2.44 ± 0.266 |
| $Na^+$ (inside PAA brushes, $\sigma_g = 1.67$ chains/$nm^2$) | 0.016 ± 0.0235 |

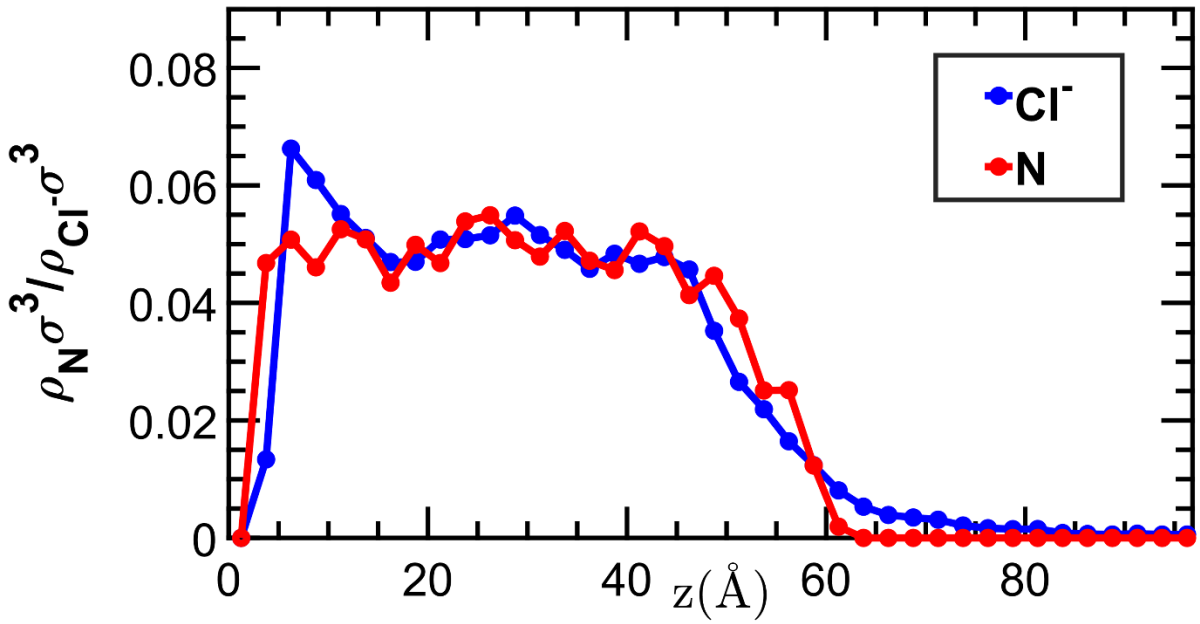


**Figure 8.** Dimensionless density distribution of the $Cl^-$ counterions and N atoms [of the $\{N(CH_3)_3\}^+$ groups] (of the PMETAC brushes) inside and outside the PMETAC brush layer (results are shown for a grafting density of 0.25 chains/nm$^2$) and the maximum uncertainty among the points reported in the plot being $\Delta\delta_{max} = \pm 0.0341\ \rho_{N/Cl^-}\sigma^3$.

## CONCLUSIONS

We have studied the microstructure of water and properties of counterions inside the PMETAC brushes using all-atom MD simulations. We reveal that inside water-solvated PMETAC brushes there are multiple water domains, centered around distinct moieties. These water domains overlap, although the specific architecture of the PMETAC brushes ensures that the water molecules inside these domains retain the influence of the moiety triggering these water domains. Water molecules in these domains demonstrate distinctly different properties that point to PMETAC brushes triggering hydrophilic hydration at one site (C=O group) and apolar hydration (with water molecules showing greater structural order) at another site ($\{N(CH_3)_3\}^+$ group). Water forms a stable intervening layer between the $\{N(CH_3)_3\}^+$ moiety and the $Cl^-$ ion, thereby preventing the $Cl^-$ ion to come in close proximity to the $\{N(CH_3)_3\}^+$ group despite strong electrostatic attraction. Such a scenario ensures a significantly high $Cl^-$ ion mobility inside the PMETAC brush layer. The C=O group of the PMETAC chain, on the other hand, demonstrates strongly hydrophilic behavior and the dipole orientation of the water molecules in the water domain around the C=O group resembles that around an anion with high charge density. Overall, our findings unravel highly intriguing water and ion behavior around a very well-studied cationic brush system and we anticipate that these findings will motivate newer discoveries and applications of PE brush grafted systems. For example, this study establishes a most unique scenario where counterions are highly mobile inside a highly charged brush layer with large grafting density: this is usually not the case for highly charged brushes. Such large mobilities of the counterions, for example, can be successfully leveraged to trigger stronger electroosmotic transport[47] and more efficient electrokinetic energy generation.[49]

## Supporting Information

MD simulation details; Results showing the time evolution and autocorrelation function of brush height; Results showing the solvation shell number, percentage and water-moiety RDF; $N(CH_3)_3^+$-$Cl^-$ and $N(CH_3)_3^+$-$O_w$ radial distribution functions (RDFs) for different grafting densities; Water dipole orientation around different moieties for different grafting densities; Tetrahedral order parameter of water around different moieties for different grafting densities.

**Acknowledgement:** This work has been supported by the Department of Energy Office of Science grant DE-SC0017741. The authors also gratefully acknowledge the Zaratan High-Performance Computing cluster at the University of Maryland for providing necessary computational resources.

**References:**


1. Zhulina, E. B.; Rubinstein, M. Lubrication by Polyelectrolyte Brushes. *Macromolecules* **2014**, *47*, 5825-5838.
2. Das, S.; Banik, M.; Chen, G.; Sinha, S.; Mukherjee, R. Polyelectrolyte Brushes: Theory, Modelling, Synthesis and Applications. *Soft Matter* **2015**, *11*, 8550-8583.
3. Chen, W. L.; Cordero, R.; Tran, H.; Ober, C. K. Polymer Brushes: Novel Surfaces for Future Materials. *Macromolecules* **2017**, *50*, 4089-4113.
4. Li, M.; Pester, C.W. Mixed Polymer Brushes for "Smart" Surfaces. *Polymers* **2020**, *12*, 1553.
5. Yang, W.; Zhou, F. Polymer Brushes for Antibiofouling and Lubrication. *Biosurface And Biotribology* **2017**, *3*, 97-114
6. Ali, M.; Yameen, B.; Cervera, J.; Ramírez, P.; Neumann, R.; Ensinger, W.; Knoll, W.; Azzaroni, O. Layer-by-layer Assembly of Polyelectrolytes into Ionic Current Rectifying Solid-state Nanopores: Insights from Theory and Experiment. *J. Am. Chem. Soc.* **2010**, *132*, 8338−8348.
7. Yameen, B.; Ali, M.; Neumann, R.; Ensinger, W.; Knoll, W.; Azzaroni, O. Single Conical Nanopores Displaying pH-Tunable Rectifying Characteristics. Manipulating Ionic Transport with Zwitterionic Polymer Brushes. *J. Am. Chem. Soc.* **2009**, *131*, 2070.
8. Ali, M.; Ramirez, P.; Mafé, S.; Neumann, R.; Ensinger, W. A pH-Tunable Nanofluidic Diode with a Broad Range of Rectifying Properties. *ACS Nano* **2009**, *3*, 603–608.
9. Cao, M.; Wang, H.; Tang, H.; Zhao, D.; Li, Y. Enzyme-Encapsulated Zeolitic Imidazolate Frameworks Formed Inside the Single Glass Nanopore: Catalytic Performance and Sensing Application. *Anal. Chem.* **2021**, *93*, 12257–12264.

10. Ali, M.; Ahmed, I.; Nasir, S.; Ramirez, P.; Niemeyer, C. M.; Mafe, S.; Ensinger, W. Ionic Transport through Chemically Functionalized Hydrogen Peroxide-Sensitive Asymmetric Nanopores. *ACS Appl. Mater. Interfaces* **2015**, *7*, 19541–19545.
11. Yang, Q.; Li, L.; Zhao, F.; Han, H.; Wang, W.; Tian, Y.; Wang, Y.; Ye, Z.; Guo, X. Hollow Silica-Polyelectrolyte Composite Nanoparticles for Controlled Drug Delivery. *J. Mater. Sci.* **2019**, *54*, 2552−2565.
12. Jiang, R.; Lu, X.; Yang, M.; Deng, W.; Fan, Q.; Huang, W. Monodispersed Brush-Like Conjugated Polyelectrolyte Nanoparticles with Efficient and Visualized SiRNA Delivery for Gene Silencing. *Biomacromolecules* **2013**, *14*, 3643–3652.
13. ShamsiJazeyi, H.; Miller, C. A.; Wong, M. S.; Tour, J. M.; Verduzco, R. Polymer-coated Nanoparticles for Enhanced Oil Recovery. *J. Appl. Polym. Sci.* **2014**, *131*, 40576.
14. Liu, G.; Cai, M.; Wang, X.; Zhou, F.; Liu, W. Core–Shell–Corona-Structured Polyelectrolyte Brushes-Grafting Magnetic Nanoparticles for Water Harvesting. *ACS Appl. Mater. Interfaces* **2014**, *6*, 11625–11632.
15. Chen, L.; Merlitz, H.; He, S.; Wu, C. X.; Sommer, J. W. Polyelectrolyte Brushes: Debye Approximation and Mean-Field Theory. *Macromolecules* **2011**, *44*, 3109–3116.
16. Borisov, O. V.; Zhulina, E. B. Conformations of Polyelectrolyte Molecular Brushes: A Mean-Field Theory. *J. Chem. Phys.* **2018**, *149*, 184904.
17. Zhulina, E. B.; Wolterink, J. K.; Borisov O. V.; Screening Effects in a Polyelectrolyte Brush: Self-Consistent-Field Theory. *Macromolecules* **2000**, *33*, 4945–4953.
18. Okrugin, B. M.; Richter, R. P.; Leermakers, F. A. M.; Neelov, I. M.; Borisov O. V.; Zhulina, E. B. Structure and Properties of Polydisperse Polyelectrolyte Brushes Studied by Self-Consistent Field Theory. *Soft Matter* **2018**, *14*, 6230-6242.

19. Sachar, H. S.; Sivasankar, V. S.; Das, S. Revisiting the Strong Stretching Theory for Ph-Responsive Polyelectrolyte Brushes: Effects of Consideration of Excluded Volume Interactions and An Expanded Form of The Mass Action Law. *Soft Matter* **2019**, *15*, 559-574.

20. Etha, S. A.; Sivasankar, V. S.; Sachar, H. S.; Das, S. Strong Stretching Theory for Ph-Responsive Polyelectrolyte Brushes in Large Salt Concentrations. *Phys. Chem. Chem. Phys.*, **2020**, *22*, 13536-13553.

21. Yu, J.; Jackson, N. E.; Xu, X.; Brettmann. B. K.; Ruths, M.; de Pablo, J. J.; Tirrell, M. Multivalent Ions induce Lateral Structural Inhomogeneities in Polyelectrolyte Brushes. *Sci. Adv.* **2017**, *3*, eaao1497.

22. Jackson, N. E.; Brettmann B. K.; Vishwanath, V.; Tirrell, T.; de Pablo, J. J. Comparing Solvophobic and Multivalent Induced Collapse in Polyelectrolyte Brushes. *ACS Macro Lett.* **2017**, *6*, 155–160.

23. Yuan, J.; Antila, S. H.; Luitjen, E. Structure of Polyelectrolyte Brushes on Polarizable Substrates. *Macromolecules* **2020**, *53*, 2983–2990.

24. Luo, Y.; Wang, C.; Pang, A.; Zhang, X.; Wang, D.; Lu, X. Low-Concentration Salt Solution Changes the Interfacial Molecular Behavior of Polyelectrolyte Brushes. *Macromolecules* **2021**, *54*, 6006–6013.

25. Elliott, I. G.; Kuhl, T. L.; Faller, R. Molecular Simulation Study of the Structure of High Density Polymer Brushes in Good Solvent. *Macromolecules* **2010**, *43*, 9131–9138.

26. Verso, F. L.; Egorov, S. A.; Milchev, A.; Binder, K. Spherical Polymer Brushes Under Good Solvent Conditions: Molecular Dynamics Results Compared to Density Functional Theory. *J. Chem. Phys.* **2010**, *133*, 184901.

27. Smook, L. A.; van Eck, G. C. R.; de Beer, S. Friends, Foes, and Favorites: Relative Interactions Determine How Polymer Brushes Absorb Vapors of Binary Solvents. *Macromolecules* **2020**, *53*, 10898-10906.

28. Mensink, L. I. S.; de Beer, S.; Snoeijer, J. H. The Role of Entropy in Wetting of Polymer Brushes. *Soft Matter* **2021**, *17*, 1368-1375.

29. Glišić. I.; Eck, G. C. R. V.; Smook, L. A.; de Beer, S. Enhanced Vapor Sorption in Block and Random Copolymer Brushes. *Soft Matter* **2022**, *18*, 8398-8405.

30. Sethuraman, V.; McGovern, M.; Morse, D. C.; Dorfman, K. D. Influence of Charge Sequence on the Adsorption of Polyelectrolytes to Oppositely-Charged Polyelectrolyte Brushes. *Soft Matter* **2019**, *15*, 5431-5442.

31. Yu, J.; Jackson, N. E.; Xu, X.; Morgenstern, M.; Kaufman, Y.; de Pablo, J. J.; Tirrell M. Multivalent Counterions Diminish the Lubricity of Polyelectrolyte Brushes. *Science* **2018**, *360*, 1434-1438.

32. Farina, R.; Laugel, N.; Pincus, P.; Tirrell, M. Brushes of Strong Polyelectrolytes in Mixed Mono- And Tri-Valent Ionic Media at Fixed Total Ionic Strengths. *Soft Matter*, **2013**, 9, 10458-10472.

33. Yu, J.; Mao, J.; Yuan, G.; Satija, S.; Chen, W.; Tirrell, M. The Effect of Multivalent Counterions To the Structure of Highly Dense Polystyrene Sulfonate Brushes. *Polymer* **2016**, *98*, 4488-453.

34. Faubel, J. L.; Patel, R. P.; Wei, W.; Curtis, J. E.; Brettmann, B. K. Giant Hyaluronan Polymer Brushes Display Polyelectrolyte Brush Polymer Physics Behavior. *ACS Macro Lett.* **2019**, *8*, 1323–1327.

35. Willott, J. D.; Humphreys, B. A.; Webber, G. B.; Wanless, E. J.; de Vos, W. M. Combined Experimental and Theoretical Study of Weak Polyelectrolyte Brushes in Salt Mixtures. *Langmuir* **2019**, *35*, 2709–2718.

36. Dahal, U. R.; Wang, Z.; Dormidontova, E. E. Hydration and Mobility of Poly(ethylene oxide) Brushes. *Macromolecules* **2017**, *50*, 6722−6732.

37. Dormidontova, E.; Chen, G. PEO-Grafted Gold Nanopore: Grafting Density, Chain Length, and Curvature Effects. *Macromolecules* **2022**, *55*, 5222–5232.

38. Dahal, U.; Dormidontova, E. Chain Conformation and Hydration of Polyethylene Oxide Grafted to Gold Nanoparticles: Curvature and Chain Length Effect. Macromolecules **2020**, *53*, 8160–8170.

39. Uehara, S.; Liu, J.; Xu, J.; Ootani, Y.; Ozawa, N.; Kubo, M. Effect of Fluorination on Friction Forces between Concentrated Polymer Brushes in the Dry State: All-atom Molecular Dynamics Simulation Study. *Chem. Lett.* **2018**, *37*, 784-786.

40. Yagasaki, T.; Matubayasi, N. Molecular Dynamics Study of the Interactions Between a Hydrophilic Polymer Brush on Graphene and Amino Acid Side Chain Analogues in Water. *Phys. Chem. Chem. Phys.* **2022**, *24*, 22877-22888.

41. Sachar, H. S.; Pial, T. H.; Desai, P. R.; Etha, S. A.; Wang, Y.; Chung, P. W.; Das, S. Densely Grafted Polyelectrolyte Brushes Trigger "Water-in-Salt"-like Scenarios and Ultraconfinement Effect. *Matter* **2020**, *2*, 1509–1521.

42. Sachar, H. S.; Pial, T. H.; Chava, B. S.; Das, S. All-atom Molecular Dynamics Simulations of Weak Polyionic Brushes: Influence of Charge Density on the Properties of Polyelectrolyte Chains, Brush-supported Counterions, and Water Molecules. *Soft Matter* **2020**, *16*, 7808-7822.

43. Sachar, H. S.; Chava, B. S.; Pial, T. H.; Das, S. All-Atom Molecular Dynamics Simulations of the Temperature Response of Densely Grafted Polyelectrolyte Brushes. *Macromolecules* **2021**, *54*, 6342–6354.

44. Sachar, H. S.; Chava, B. S.; Pial, T. H.; Das, S. Hydrogen Bonding and Its Effect on the Orientational Dynamics of Water Molecules inside Polyelectrolyte Brush-Induced Soft and Active Nanoconfinement. *Macromolecules* **2021**, *54*, 2011–2021.

45. Pial, T. H.; Sachar, H. S.; Das, S. Quantification of Mono- and Multivalent Counterion-Mediated Bridging in Polyelectrolyte Brushes. *Macromolecules* **2021**, *54*, 4154–4163.

46. Pial, T. H.; Prajapati, M.; Chava, B. S.; Sachar, H. S.; Das, S. Charge-Density-Specific Response of Grafted Polyelectrolytes to Electric Fields: Bending or Tilting?. *Macromolecules* **2022**, *55*, 2413–2423.

47. Pial, T. H.; Sachar, H. S.; Desai, P. R.; Das, S. Overscreening, Co-Ion-Dominated Electroosmosis, and Electric Field Strength Mediated Flow Reversal in Polyelectrolyte Brush Functionalized Nanochannels. *ACS Nano* **2021**, *15*, 6507–6516.

48. Pial, T. H.; Das, S. Specific Ion and Electric Field Controlled Diverse Ion Distribution and Electroosmotic Transport in a Polyelectrolyte Brush Grafted Nanochannel. *J. Phys. Chem. B* **2022**, *126*, 10543−10553.

49. Sachar, H. S.; Pial, T. H.; Sivasankar, V. S.; Das, S. Simultaneous Energy Generation and Flow Enhancement (Electroslippage Effect) in Polyelectrolyte Brush Functionalized Nanochannels. *ACS Nano* **2021**, *15*, 17337–17347.

50. Pial, T. H.; Das, S. Machine Learning Enabled Quantification of the Hydrogen Bonds Inside the Polyelectrolyte Brush Layer Probed Using All-Atom Molecular Dynamics Simulations. *Soft Matter* **2022**, *18*, 8945−8951.

51. Santos, D. E. S.; Li, D.; Ramstedt, M.; Gautrot, J. E.; Soares, T. A. Conformational Dynamics and Responsiveness of Weak and Strong Polyelectrolyte Brushes: Atomistic Simulations of Poly (Dimethyl Aminoethyl Methacrylate) and Poly(2-(Methacryloyloxy)Ethyl Trimethylammonium Chloride). *Langmuir* **2019,** *35*, 5047-5049.
52. Wu, B.; Wang, X.; Yang, J.; Hua, Z.; Tian, K.; Kou, R.; Zhang, J.; Ye, S.; Luo, Y.; Craig, V. S. J.; Zhang, G.; Liu, G. Reorganization of Hydrogen Bond Network Makes Strong Polyelectrolyte Brushes Ph-Responsive. *Sci. Adv.* **2016**, *2*, e1600579.
53. Chu, X.; Yang, J.; Liu, G.; Zhao, J. Swelling Enhancement of Polyelectrolyte Brushes Induced By External Ions. *Soft Matter* **2014**, *10*, 5568-5578.
54. Dahal, U.; Dormidontova, E. E. Chain Conformation and Hydration of Polyethylene Oxide Grafted to Gold Nanoparticles: Curvature and Chain Length Effect. *Macromolecules* **2020**, *53*, 8160–8170.
55. Thompson, A. P.; Aktulga, H. M.; Berger, R.; Bolintineanu, D. S.; Brown, W. M.; Crozier, P. S.; in 't Veld, P. J.; Kohlmeyer, A.; Moore, S. G.; Nguyen, T. D.; Shan, R.; Stevens, M. J.; Tranchida, J.; Trott, C.; Plimpton, S. J. LAMMPS - A Flexible Simulation Tool For Particle-Based Materials Modeling At The Atomic, Meso, And Continuum Scales. *Comput. Phys. Commun.* **2022**, *271*, 108171.
56. Jewett, A. I.; Stelter, D.; Lambert, J.; Saladi, S. M.; Roscioni, O. M.; Ricci, M.; Autin, L.; Maritan, M.; Bashusqeh, S. M.; Keyes, T.; Dame, R. T.; Shea, J. E.; Jensen, G. J.; Goodsell, D. S. Moltemplate: A Tool for Coarse-Grained Modeling of Complex Biological Matter and Soft Condensed Matter Physics. *J. Mol. Biol.* **2021**, *433*, 166841.

57. Jorgensen, W. L.; Maxwell, D. S.; Tirado-Rives, J. Development and Testing of the OPLS All-Atom Force Field on Conformational Energetics and Properties of Organic Liquids. *J. Am. Chem. Soc.* **1996**, *118*, 11225–11236.

58. Pial, T. S.; Das, S. Machine Learning Enabled Quantification of The Hydrogen Bonds Inside the Polyelectrolyte Brush Layer Probed Using All-Atom Molecular Dynamics Simulations. *Soft Matter* **2022**, *18*, 8945-8951.

59. Ghobadi, A. F.; Jayaraman, A. Effects of Polymer Conjugation on Hybridization Thermodynamics of Oligonucleic Acids. *J. Phys. Chem. B* **2016**, *120*, 9788–9799.

60. Joung, I. S.; Cheatham, T. E. III. Determination of Alkali and Halide Monovalent Ion Parameters for Use in Explicitly Solvated Biomolecular Simulations. *J. Phys. Chem. B* **2008**, *112*, 9020–9041.

61. Csajka, F. S.; Seidel, C. Strongly Charged Polyelectrolyte Brushes: A Molecular Dynamics Study. *Macromolecules* **2000**, *33*, 2728–2739.

62. Turner, J.; Soper, A. K.; Finney, J. L. A Neutron-Diffraction Study of Tetramethylammonium Chloride In Aqueous Solution. *Mol. Phys.* **1990**, *70*, 679-700.

63. Hawlicka, E.; Dlugoborski, T. Molecular Dynamics Simulations of The Aqueous Solution of Tetramethylammonium Chloride. *Chem. Phys. Lett.* **1997**, *268*, 325-330.

64. García-Tarrés, L.; Guàrdia, E. Hydration and Dynamics of a Tetramethylammonium Ion in Water: A Computer Simulation Study. *J. Phys. Chem. B* **1998**, *102*, 7448–7454.

65. Biswas, A.; Priyadarshini, A.; Malik, B. S. Dynamics and Spectral Response of Water Molecules around Tetramethylammonium Cation. *J. Phys. Chem. B* **2019**, *123*, 8753–8766.

66. Mancinelli, R.; Botti, A.; Bruni, F.; Ricci, M. A.; Soper, A. K. Hydration of Sodium, Potassium, and Chloride Ions in Solution and the Concept of Structure Maker/Breaker. *J. Phys. Chem. B* **2007**, *111*, 13570–13577.

67. Vaisman, I. I.; Brown, F. K.; Tropsha, A. Distance Dependence of Water Structure around Model Solutes. *J. Phys. Chem.* **1994**, *98*, 5559–5564.

68. Zhou, J.; Lu, X.; Wang, Y.; Shi, J. Molecular Dynamics Study on Ionic Hydration. *Fluid Phase Equilib.* **2002**, *194-197*, 257-270.

69. Nilsson, E. J.; Alfredsson, V.; Bowron, D. T.; Edler, K. J. A Neutron Scattering and Modelling Study of Aqueous Solutions of Tetramethylammonium and Tetrapropylammonium Bromide. *Phys. Chem. Chem. Phys.,* **2016***,18,* 11193-11201.

70. Van der post, S. T.; Scheidelaar, S.; Bakker, H. J. Water Dynamics in Aqueous Solutions of Tetra-n-alkylammonium Salts: Hydrophobic and Coulomb Interactions Disentangled. *J. Phys. Chem. B* **2013**, *117*, 15101–15110.

71. Turner, J. Z.; Soper, A. K.; Finney, J. L. Ionic versus Apolar Behavior of the Tetramethylammonium Ion in Water. *J. Chem. Phys.* **1995**, *102*, 5438–5443.

72. Duboué-Dijon, E.; Laage, D. Characterization of the Local Structure in Liquid Water by Various Order Parameters. *J. Phys. Chem. B* **2015**, *119*, 8406–8418.

73. Varanasi, S. R.; Guskova, O. A.; John, A.; Sommer, J.-U. Water around Fullerene Shape Amphiphiles: A Molecular Dynamics Simulation Study of Hydrophobic Hydration. *J. Chem. Phys.* **2015**, *142*, 224308.

74. Coe, M. K.; Evans, R.; Wilding, N. B. Understanding the Physics of Hydrophobic Solvation. *J. Chem. Phys.* **2023**, *158*, 034508.

75. Grabowska, J.; Kuffel, A.; Zielkiewicz, J. Revealing the Frank–Evans "Iceberg" Structures within the Solvation Layer around Hydrophobic Solutes. *J. Phys. Chem. B* **2021**, *125*, 1611–1617.

76. Frank, H. S.; Evans, M. W. Free Volume and Entropy in Condensed Systems III. Entropy in Binary Liquid Mixtures; Partial Molal Entropy in Dilute Solutions; Structure and Thermodynamics in Aqueous Electrolytes. *J. Chem. Phys.* 1945, *13*, 507-532.

77. Montagna, M.; Sterpone, F.; Guidoni, L. Structural and Spectroscopic Properties of Water around Small Hydrophobic Solutes. *J. Phys. Chem. B* **2012**, *116*, 11695–11700.

78. Jerie, K., Baranowski, A., Jákli, G.; Gliński, J. Structure of Aqueous Solutions of Tetraethylammonium Chloride Investigated by Positron Annihilation and Ultrasonic Methods. *J. Radioanal. Nucl. Chem.* **1999**, *240*, 223–229.

79. Galamba, N. Water's Structure Around Hydrophobic Solutes and the Iceberg Model. *J. Phys. Chem. B* **2013**, *117*, 2153–2159.

80. Strazdaite, S.; Versluis, J.; Backus, E. H. G.; Bakker, H. J. Enhanced Ordering of Water at Hydrophobic Surfaces. *J. Chem. Phys.* **2014**, *140*, 054711.

81. Kowsari, M. H.; Alavi, S.; Ashrafizadeeh, M.; Najafi, B. Molecular Dynamics Simulation of Imidazolium-based Ionic Liquids. 1. Dynamics and Diffusion Coefficient. *J. Chem. Phys.* **2008**, *129*, 224508.

# Hydrophilic and Apolar hydration in Densely Grafted Cationic Brushes and Counterions with Large Mobilities: Supporting Information

Raashiq Ishraaq,[1] Tanmay Sarkar Akash,[1] Arka Bera,[1] and Siddhartha Das[1*]

[1]Department of Mechanical Engineering, University of Maryland, College Park, MD 20742

*Corresponding Author Email: sidd@umd.edu

## S1. MD simulation details:

### S1.1. Model of the PMETAC monomers

The model of the PMETAC monomers used in our simulations has been shown in Fig. S1.

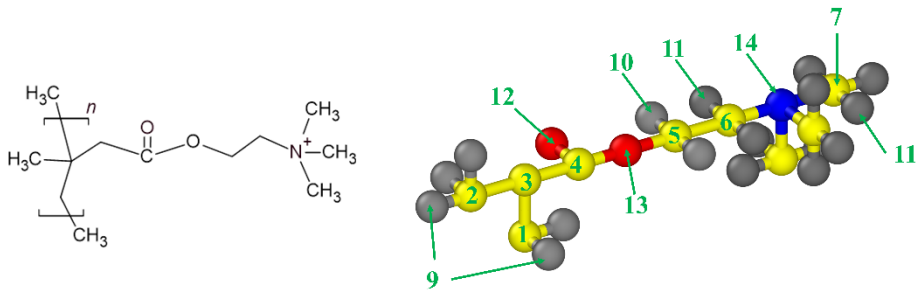


(a) (b)

**Figure S1:** (a) Chemical structure of a PMETAC monomer. (b) Model of a PMETAC monomer used in this simulation. Yellow, red, blue and grey atoms respectively represent carbon, oxygen, nitrogen and hydrogen. The number represents the atom type number used to refer atoms in this study.

### S1.2. Nonbonded interaction terms:

OPLS-AA forcefield [1] parameters were used to model the interaction between the atoms of the brush.[2] Parameters from the study of Joung et al.[2,3] were used for modeling the counterion interactions. The parameters can be found in the website (see Ref. 4) and were first distributed with Enhanced Monte Carlo package.[5] SPC/E water model was used as an explicit solvent. The expression for the total energy of the system ($U_{total}$) is provided in Eq. (S1), with

$U_{LJ}, U_{Coul}, U_{Bond}, U_{Angle}, U_{Dihedral}$ and $U_{Improper}$ correspondingly representing the Lennard-Jones (LJ), Coulomb, bond, angle, dihedral, and improper interaction energies.

$$U_{total} = U_{LJ} + U_{Coul} + U_{Bond} + U_{Angle} + U_{Dihedral} + U_{Improper}. \quad \text{(S1)}$$

The expressions of the LJ and the Coulomb interaction energies between the $i^{th}$ and $j^{th}$ atoms are respectively provided in Eqs. S2 and S3.

$$U_{LJ} = 4\epsilon_{ij}\left[\left(\frac{\sigma_{ij}}{r_{ij}}\right)^{12} - \left(\frac{\sigma_{ij}}{r_{ij}}\right)^{6}\right] \quad \text{(S2)}$$

$$U_{Coul} = \frac{q_i q_j}{4\pi \epsilon_1 \epsilon_0 r_{ij}} \quad \text{(S3)}$$

In these equations, $\epsilon_{ij}, r_{ij}$ , $\sigma_{ij}, q_i$ and $q_j$respectively represents the energy well depth, distance, zero-interaction energy distance, the charge of the $i^{th}$ atom, and the charge of the $j^{th}$atom. $\epsilon_0$ and $\epsilon_1$ respectively represents the permittivity of the vacuum and the relative permittivity of the background (here used as 1). All the parameters for the different atom types have been provided in table S1. The LJ interactions between dissimilar atom types were found using geometric mixing rules except for ion-water and ion-ion interaction, where the Lorentz-Berthelot mixing rules were used to be consistent with Joung et al.[3]

**Table S1:** Parameters for the different atom types needed for calculating the LJ and Coulomb interactions

| **Atom Type (OPLS type)** | **Charge(e)** | **Mass(amu)** | **ϵ(Kcal/mole)** | **σ(Å)** |
|---|---|---|---|---|
| 1 (C1) | -0.12 | -12.011 | 0.066 | 3.50 |

| | | | | |
|---|---|---|---|---|
| 2 (C2) | -0.18 | 12.011 | 0.066 | 3.50 |
| 3 (C3) | 0.0 | 12.011 | 0.066 | 3.50 |
| 4 (C4) | 0.51 | 12.011 | 0.105 | 3.75 |
| 5 (C5) | 0.19 | 12.011 | 0.066 | 3.50 |
| 6 (C6) | 0.05 | 12.011 | 0.066 | 3.50 |
| 7 (C7) | -0.05 | 12.011 | 0.066 | 3.50 |
| 8 (End carbon-C2) | -0.18 | 12.011 | 0.066 | 3.50 |
| 9 (H1) | 0.06 | 1.008 | 0.030 | 2.50 |
| 10 (H2) | 0.03 | 1.008 | 0.015 | 2.42 |
| 11 (H3) | 0.1 | 1.008 | 0.030 | 2.50 |
| 12 (O1) | -0.430 | 15.999 | 0.210 | 2.960 |
| 13 (O2) | -0.330 | 15.999 | 0.170 | 3.000 |
| 14 (N) | 0.0 | 14.007 | 0.170 | 3.250 |
| 15 ($O_w$) | -0.8476 | 15.999 | 0.155354 | 3.166 |
| 16 ($H_w$) | 0.4238 | 1.008 | 0 | 0 |
| 17 (Cl) | -1.00 | 35.453 | 0.012785 | 4.83 |
| LJ wall (remains the same with all types of atoms) | 0.00 | 15.00794 | 0.1947 | 3.00 (LJ cut off length is 3.36 Å) |

Bond interaction energy is modeled using harmonic style potential as depicted by Eq. S4.

$$U_{Bond} = K_{b,ij}(r_{ij} - r_{0,ij})^2 \quad \text{(S4)}$$

Here $K_{b,ij}$ and $r_{0,ij}$ denotes respectively the bond stiffness and the equilibrium bond length between the $i^{th}$ and $j^{th}$ atom. The values of these constants ($K_b$ and $r_0$) for different atom combination have been provided in Table S2.

**Table S2:** Values of the parameters ($K_b$ and $r_0$) for different atom combination used to calculate Bond interaction energy.

| **Bond Type (Participating atoms)** | $\boldsymbol{K_b}$, $(\frac{\boldsymbol{Kcal}}{\boldsymbol{mol}.\text{Å}^2})$ | **$r_0$(Å)** |
|---|---|---|
| 1-9 | 340 | 1.09 |
| 1-3 | 268 | 1.529 |
| 2-3 | 268 | 1.529 |
| 2-9 | 340 | 1.09 |
| 3-4 | 317 | 1.522 |
| 4-12 | 570 | 1.229 |
| 4-13 | 214 | 1.327 |
| 5-13 | 320 | 1.41 |
| 5-6 | 268 | 1.529 |
| 5-10 | 340 | 1.09 |
| 6-11 | 340 | 1.09 |
| 6-14 | 367 | 1.471 |
| 7-14 | 367 | 1.471 |
| 7-11 | 340 | 1.09 |

| | | |
|---|---|---|
| 8-3 | 268 | 1.529 |
| 8-9 | 340 | 1.09 |
| 15-16 | 0 | 1 |

The expression for the angle interaction energy between three atoms ($i, j$ and $k$) that are connected by bonds is provided in Eq. S5.

$$U_{Angle} = K_{a,ijk}(\theta_{ij} - \theta_{0,ijk})^2 \quad \text{(S5)}$$

The angle interaction energy is also modeled as harmonic. $K_{a,ijk}$ and $\theta_{0,ijk}$ in eq.(S5) respectively represent the angle stiffness and the equilibrium value of the angle (for the case where the angle is formed between three atoms *i, j*, and *k*) and their values have been provided in Table S3.

**Table S3:** Values of the parameters ($K_a$ and $\theta_0$) for different three-atom combinations used to calculate angle interaction energy.

| **Angle Type** | $\boldsymbol{K_a, (\frac{Kcal}{mol.rad^2})}$ | $\boldsymbol{\theta_0(deg)}$ |
|---|---|---|
| 9-1-9 | 33 | 107.8 |
| 9-1-3 | 37.5 | 110.7 |
| 9-8-9 | 33 | 107.8 |
| 9-8-3 | 37.5 | 110.7 |
| 1-3-2 | 58.35 | 112.7 |
| 1-3-1 | 58.35 | 112.7 |

| | | |
|---|---|---|
| 3-1-3 | 58.35 | 112.7 |
| 1-3-4 | 63 | 111.1 |
| 2-3-4 | 63 | 111.1 |
| 8-3-2 | 58.35 | 112.7 |
| 8-3-1 | 58.35 | 112.7 |
| 8-3-4 | 63 | 111.1 |
| 9-2-3 | 37.5 | 110.7 |
| 9-2-9 | 33 | 107.8 |
| 3-4-12 | 80 | 120.4 |
| 3-4-13 | 81 | 111.4 |
| 12-4-13 | 83 | 123.4 |
| 4-13-5 | 83 | 116.9 |
| 10-5-13 | 35 | 109.5 |
| 6-5-13 | 50 | 109.5 |
| 10-5-10 | 33 | 107.8 |
| 10-5-6 | 37.5 | 110.7 |
| 5-6-11 | 37.5 | 110.7 |
| 5-6-14 | 80 | 111.2 |
| 11-6-14 | 35 | 109.5 |
| 6-14-7 | 50 | 113 |
| 11-6-11 | 33 | 107.8 |
| 11-7-11 | 33 | 107.8 |

| | | |
|---|---|---|
| 11-7-14 | 35 | 109.5 |
| 7-14-7 | 50 | 113 |
| 16-15-16 | 0 | 109.47 |

The Dihedral interaction energy between four consecutively connected atoms ($i, j, k$ and $l$) is provided in Eq. S6.

$$U_{Dihedral} = \frac{1}{2}K_1[1 + \cos(\emptyset)] + \frac{1}{2}K_2[1 - \cos(2\emptyset)] + \frac{1}{2}K_3[1 + \cos(3\emptyset)] + \frac{1}{2}K_4[1 - \cos(4\emptyset)]. \quad \text{(S6)}$$

In eq.(S6), $K_1, K_2, K_3$, and $K_4$ denote the Fourier coefficients, while $\emptyset$ denotes the torsion angle. Table S4 lists these parameters for different combinations of the consecutively connected atoms.

**Table S4:** Values of the parameters ($K_1, K_2, K_3$, and $K_4$) used to calculate the dihedral interaction energy between four consecutively connected atoms

| **Dihedral type** | $\boldsymbol{K_1}$, $(\boldsymbol{Kcal/mole})$ | $\boldsymbol{K_2}$, $(\boldsymbol{Kcal/mole})$ | $\boldsymbol{K_3}$, $(\boldsymbol{Kcal/mole})$ | $\boldsymbol{K_4}$, $(\boldsymbol{Kcal/mole})$ |
|---|---|---|---|---|
| 9-1-3-1 | 0 | 0 | 0.3 | 0 |
| 9-1-3-2 | 0 | 0 | 0.3 | 0 |
| 9-8-3-1 | 0 | 0 | 0.3 | 0 |
| 9-8-3-2 | 0 | 0 | 0.3 | 0 |
| 9-1-3-4 | 0 | 0 | -0.076 | 0 |
| 9-8-3-4 | 0 | 0 | -0.076 | 0 |
| 1-3-1-3 | 1.3 | -0.05 | 0.2 | 0 |

| | | | | |
|---|---|---|---|---|
| 1-3-2-9 | 0 | 0 | 0.3 | 0 |
| 1-3-4-12 | -0.2777 | 1.228 | -0.694 | 0 |
| 1-3-4-13 | 0 | 0 | -0.553 | 0 |
| 8-3-1-3 | 1.3 | -0.05 | 0.2 | 0 |
| 8-3-2-9 | 0 | 0 | 0.3 | 0 |
| 8-3-4-12 | -0.2777 | 1.228 | -0.694 | 0 |
| 8-3-4-13 | 0 | 0 | -0.553 | 0 |
| 9-2-3-4 | 0 | 0 | -0.076 | 0 |
| 2-3-4-12 | -0.2777 | 1.228 | -0.694 | 0 |
| 2-3-4-13 | 0 | 0 | -0.553 | 0 |
| 2-3-1-3 | 1.3 | -0.05 | 0.2 | 0 |
| 3-1-3-4 | -1.697 | -0.456 | 0.585 | 0 |
| 3-4-13-5 | 4.669 | 5.124 | 0 | 0 |
| 12-4-13-5 | 0 | 5.124 | 0 | 0 |
| 4-13-5-10 | 0 | 0 | 0.198 | 0 |
| 4-13-5-6 | -1.22 | -0.126 | 0.422 | 0 |
| 13-5-6-11 | 0 | 0 | 0.468 | 0 |
| 13-5-6-14 (from ref. 6) | 1.2997 | -0.05 | 0.2 | 0 |
| 10-5-6-11 | 0 | 0 | 0.3 | 0 |
| 10-5-6-14 | 0 | 0 | 0.384 | 0 |
| 5-6-14-7 | 1.4379 | -0.1238 | 0.2639 | 0 |
| 11-6-14-7 | 0 | 0 | 0.3017 | 0 |

| | | | | |
|---|---|---|---|---|
| 11-7-14-7 | 0 | 0 | 0.3017 | 0 |
| 6-14-7-11 | 0 | 0 | 0.3017 | 0 |
| 9-1-3-8 | 0 | 0 | 0.3 | 0 |

Finally, the improper interaction energy is expressed in eq.(S7):

$$U_{improper} = K_{\text{ijkl}}(\psi - \psi_0)^2. \quad \text{(S7)}$$

In eq.(S7), $K_{\text{ijkl}}$ and $\psi_0$ denote the torsional stiffness and equilibrium improper torsional angle. The values of these parameters for different atom combinations have been provided in table S5.

**Table S5:** Values of the parameters ($K_i$ and $\psi_0$) used to calculate the improper interaction energy between four consecutively connected atoms

| **Improper Type** | $K_i$ $(\frac{Kcal}{mol.rad^2})$ | $\psi_0$ (degrees) |
|---|---|---|
| 4-13-3-12 | 10.5 | 180 |

## S2. Time evolution and autocorrelation function of brush height

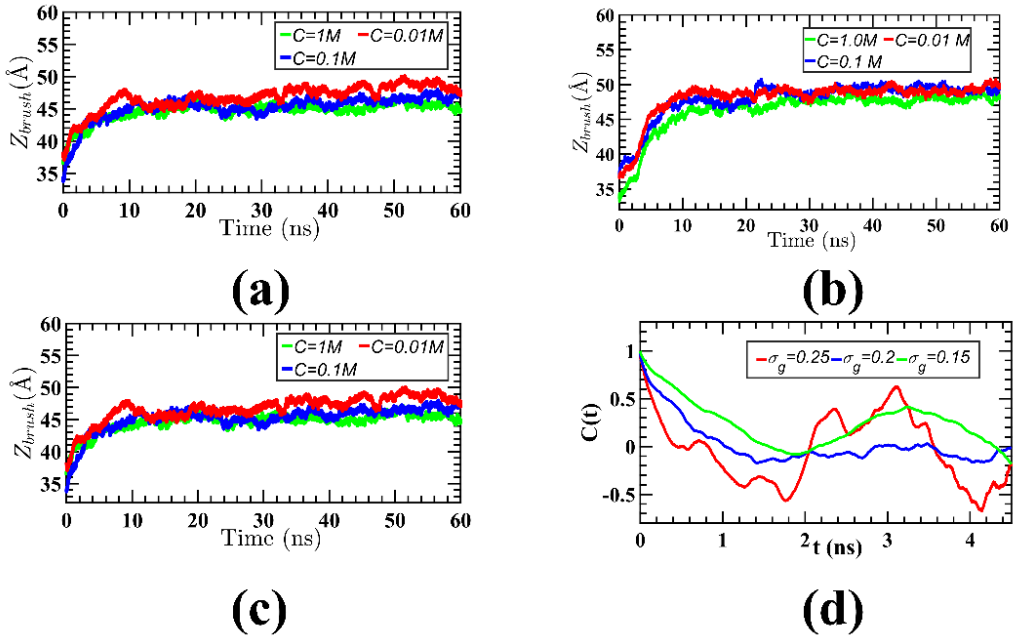


**Figure S2:** Brush height evolution profile for (a) $\sigma_g$=0.25 chain/nm$^2$ (b) $\sigma_g$=0.20 chain/nm$^2$ (c) $\sigma_g$=0.15 chain/nm$^2$, where $\sigma_g$ denotes the grafting density. In the legends of sub-figures (a-c), *C* denotes the concentration of external salt (NaCl) in molarity. The brush height is defined as the distance (both time and chain averaged) between the z-coordinates of the top and grafting carbons of the backbone polymer, as defined by the following formula: $Z_{brush} = \langle z_{top} - z_{graft} \rangle_{time\ and\ chain\ average}$. Here, $Z_{brush}$, $z_{top}$, and $z_{graft}$ respectively denote the brush height, the z-coordinates of the top carbons, and the z-coordinates of the brush grafting carbons.[7] The square bracket (<>) means averaging over all chains and timesteps. (d) Autocorrelation function of average brush height for different grafting densities. Fluctuations of the brush height is one of the slowest dynamics of brush systems (due to confinement). The decay time of the autocorrelation functions are almost an order of magnitude lesser than the production run (12 ns) thus necessitating

sufficient statistical sampling. The autocorrelation function was calculated using the following equation: $C(t') = \frac{[f(t)-\langle f\rangle][f(t+t')-\langle f\rangle]}{\sigma_f^2}$. Here C($t'$), $\sigma_f$ and $t'$ are the correlation coefficient, standard deviation, and the lag time. The *x*-axis shown in part (d) is the lag time ($t'$) and not the trajectory time ($t$). The purpose of plotting the autocorrelation function is to see after what amount of time an observable loses its memory (i.e., the auto correlation function goes to zero). For our cases, we can see that far before a lagtime of 4 ns, C($t'$) corresponding to the brush height for all the different grafting density values goes to zero. This oscillatory autocorrelation behavior of the brush height has been shown to occur (for PE brush height) in other studies probing the behavior PE brushes (for other types of PE brushes) using coarse-grained simulations.[8]

## S3. Solvation shell number, percentage and water-moiety RDF

### S3.1. Radial distribution function of water around different moieties

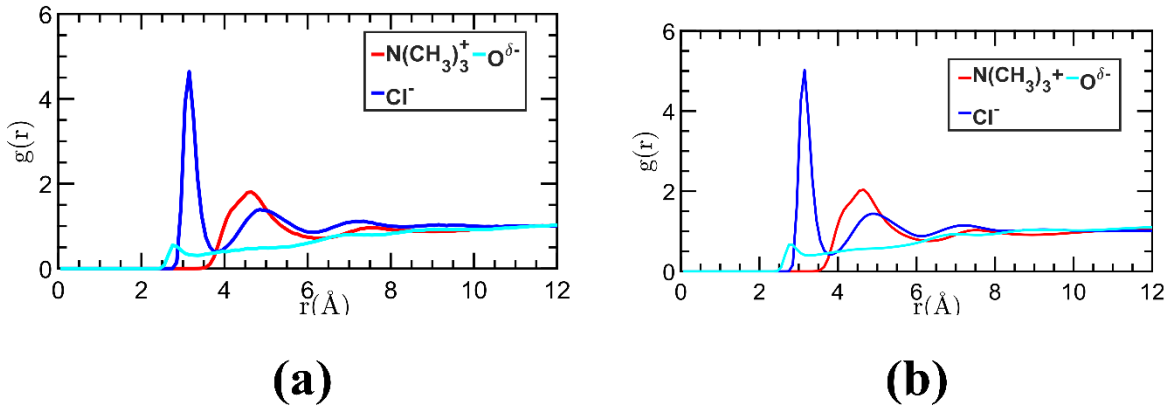


**Figure S3:** Radial distribution function with $O_w$ (oxygen of water) with different Moieties of the brush for (a) $\sigma_g$=*0.15* chains/nm$^2$ and (b) $\sigma_g$=*0.20* chains/nm$^2$. Here $\sigma_g$ denotes the grafting density. The RDF matches with previous simulations and experiment.[9-11]

**S3.2. Solvation shell percentage**

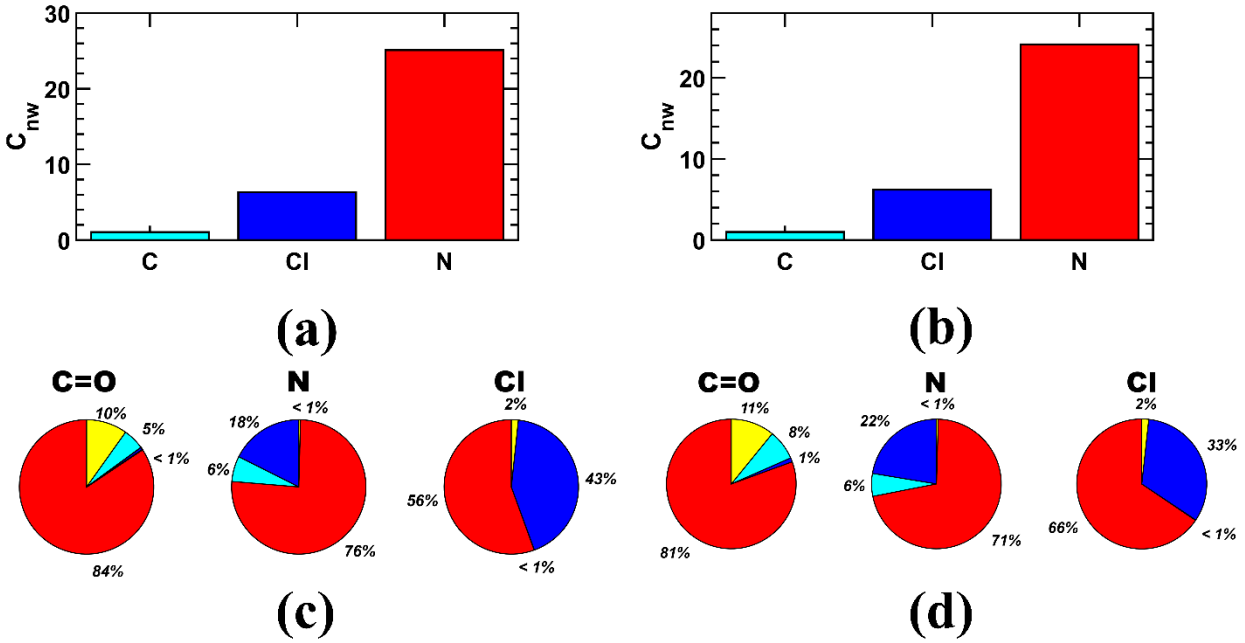


**Figure S4:** Solvation number of different moieties for (a) $\sigma_g$=*0.15* chains/nm$^2$ and (b) $\sigma_g$=*0.20* chains/nm$^2$. Here $\sigma_g$ denotes the grafting density. Pie chart showing the overlap of solvation shell of different moieties in percentage for (c) $\sigma_g$=*0.15* chains/nm$^2$ and (d) $\sigma_g$=*0.20* chains/nm$^2$. To quantify the solvation shell radius for each moiety (which defines the "water domain" centered around each moiety), we first calculated the RDF between water oxygen ($O_w$) and X, where X is N, C or $Cl^-$ depending on the moiety. Then the domain (of each moiety) was defined as the region characterized by the distance from 0 to the first minima of the $O_w$-Moiety RDF. Despite significant overlap of these domains formed around different moieties, these moieties manage to maintain their characteristic influence on the surrounding water structure. The solvation number was calculated by counting the average number of water molecules present around each moiety with in the solvation shell radius.

## S4. $N(CH_3)_3^+$-$Cl^-$ and $N(CH_3)_3^+$-$O_w$ radial distribution functions (RDFs)

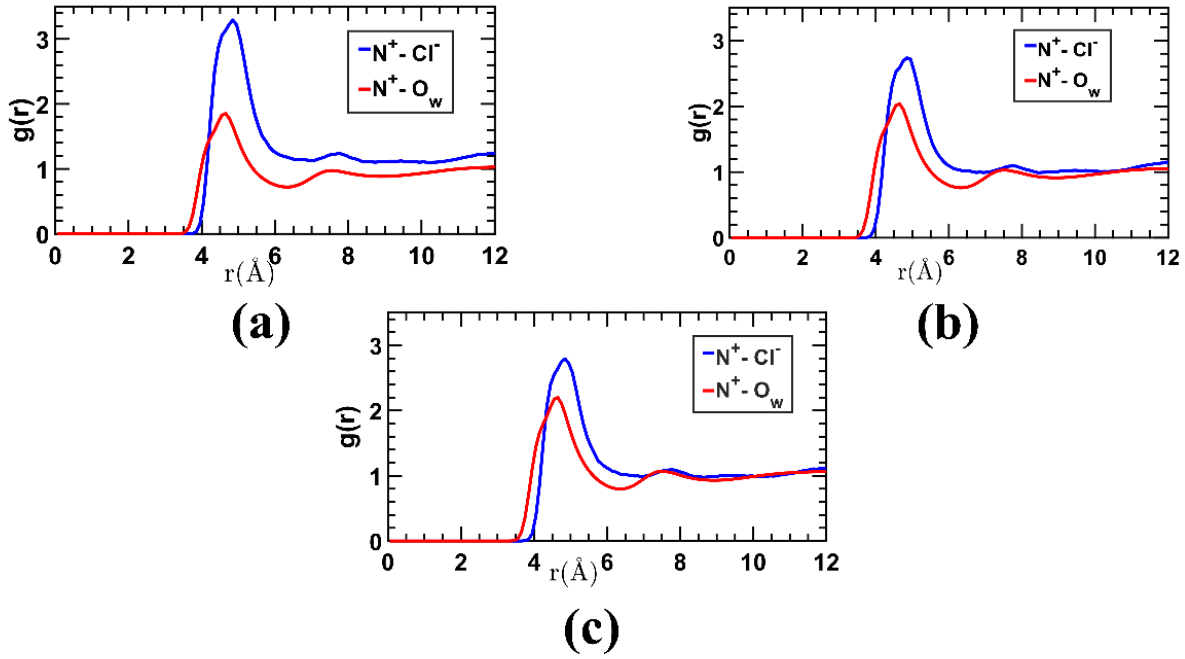


**Figure S5:** $N(CH_3)_3^+$-$Cl^-$ and $N^+$-$O_W$ RDFs for (a) $\sigma_g$=*0.15* chains/nm$^2$, (b) $\sigma_g$=*0.20* chains/nm$^2$, and (c) $\sigma_g$=*0.25* chain/nm$^2$. Here $\sigma_g$ denotes the grafting density.

## S5. Water dipole orientation around different moieties

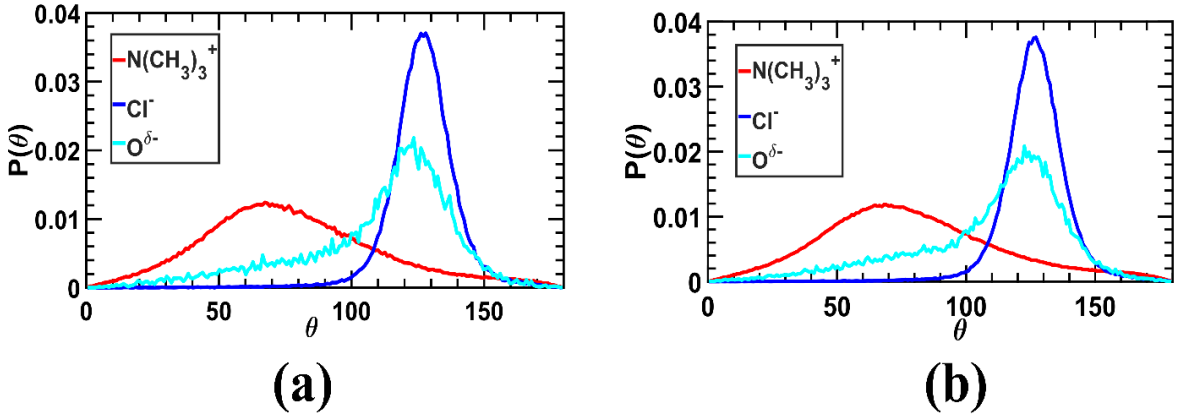


**Figure S6:** Water dipole orientation around different moieties for (a) $\sigma_g$=*0.15* chains/nm$^2$ and (b) $\sigma_g$=*0.20* chains/nm$^2$. $\sigma_g$ denotes the grafting density.

## S6. Tetrahedral order parameter of water around different moieties:

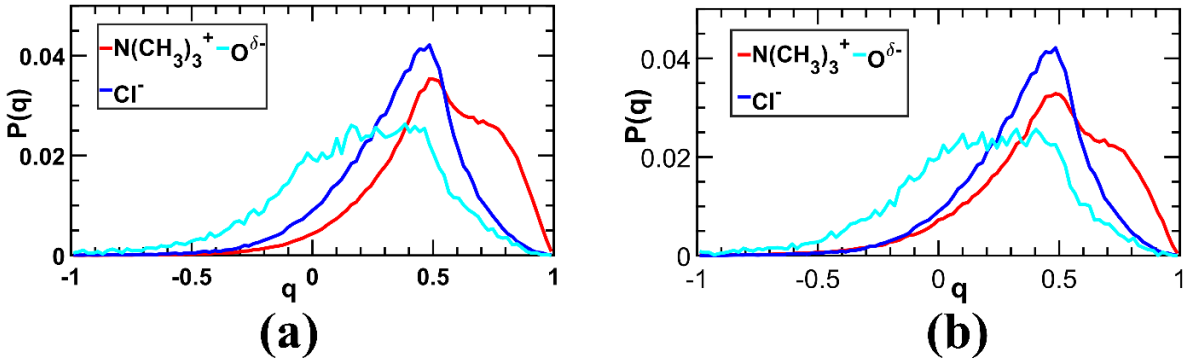


**Figure S7:** Tetrahedral water parameter around different moieties (a) $\sigma_g$=*0.15* chains/nm$^2$ and (b) $\sigma_g$=*0.20* chains/nm$^2$. $\sigma_g$ denotes the grafting density.

The tetrahedral order parameter is calculated using eq.(S8), as shown below[12]:

$$q_i = 1 - \frac{3}{8}\sum_{j=1}^{3}\sum_{k=j+1}^{4}\left(Cos\theta_{ijk} + \frac{1}{3}\right)^2 \qquad \text{(S8)}.$$

Here i denotes the center particle for which the q parameter is calculated and the j,k are the vertices of the tetrahedron. A typical orientation of water in a tetrahedral formation is shown in Fig S8(a) (only the oxygen atoms are shown for clarity). Here, i denotes the central atom (green) and 1,2,3,4 denotes the rest of the vertices (red). The angles of the tetrahedron are: 1-i-2, 1-i-3, 1-i-4, 2-i-3, 2-i-4, and 3-i-4 (six angles), which are the $\theta_{ijk}$ values of eq.(S8). The range of the "q" parameter varies from -3 to 1 [see Fig. S8(b)], as has been shown in our previous study[13] (though only from -1 to 1 is plotted) and other studies[14]. This function gives a score to the central oxygen particle (green) based on how close its local environment is to an ice-like structure. If the other four oxygen atoms (red) are arranged in a perfect tetrahedron (like ice) around the central oxygen atoms, then

the value of "q" of the corresponding central particle (green) is 1 and the water arrangement is said to be in a perfect tetrahedral.

To determine the structural order of the water molecules inside the hydration shell, one must ask the question "*How well the water molecules (or hydration shell water molecules of a given solute) wrap around among themselves in a tetrahedral arrangement?*". Calculating the "q" values of the water molecules of the first hydration shell answers this question.[15-17] Fig S9 shows a typical arrangement of four water molecules near a solute, where again the green atom denotes the central particle for which q parameter is calculated and the other atoms are red. The three water molecules (red) of the tetrahedral base and the central particle (green) are all first hydration shell water molecules. The q parameter value of the central particle gives us information about the tetrahedral-like arrangement of the base atoms (arrangement of the water molecules of the first hydration layer among themselves). Since it is a 3D structure, and not a 2D one, the water molecules can wrap around the spherical solute and can also attain a tetrahedral-like arrangement. If the *q* parameter values are high, we can infer that the solvation shell water molecules are in a more ordered arrangement ***among themselves***. If one aims to calculate how far from a solute the effect of the solute on the "q" parameter lasts, it becomes necessary to study the second peak of the q parameter distribution associated with the solute-bound water.[18] The information we are looking at here is completely different, which is how well the water molecules (of the first hydration layer) are in an ordered structure among themselves.

In our case, *q* parameter further sheds light on the effect of increasing the grafting density. For example, when the brush grafting densities are increased from 0.15 to 0.25, the percentage of shared water molecules [between $Cl^-$ ion and $(N(CH_3)_3)^+$ moiety] of the first hydration shell increases [compare Fig. 4(c) in the main paper with Figs. S4(c,d)], which results in a decrease of

the “q” parameter value (see inset Fig. 6 of main paper) of the waters in the first solvation shell of the moiety of interest. This information allows us to infer that the moiety [in our case $\{N(CH_3)_3)^+\}$] enables the creation of an ordered water structure (clathrate-like) on its own, which is also commensurate with our inference that the $\{N(CH_3)_3)^+\}$ moiety triggers hydrophobic hydration effects. Therefore, calculating “q” parameter value of the water molecules of the first hydration shell has great significance for our case.

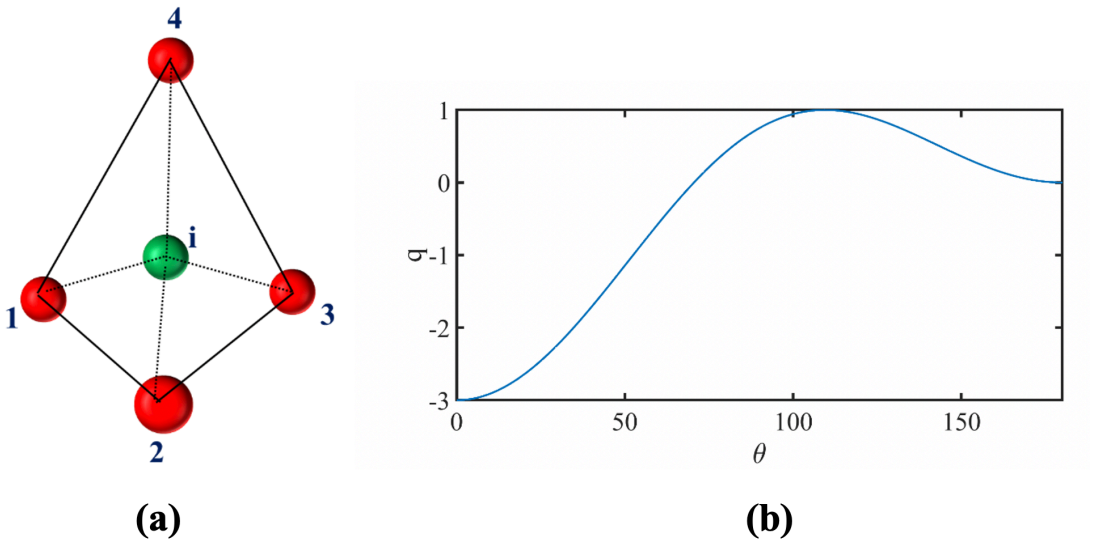


**Figure S8:** (a) A schematic representation showing a tetrahedral arrangement of water molecules (only oxygen molecules are shown for clarity). (b) Shows the range of value for the q parameter for the case where the the tetrahedral angle (θ) between three atom j,i, k (where i is the central atom) varies from 0 to 180 degrees.

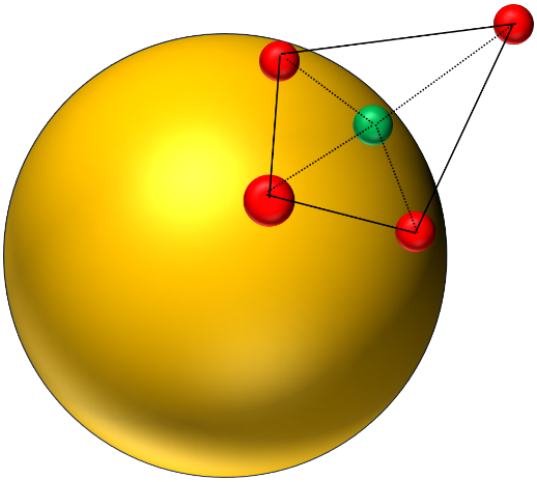

**Figure S9:** Arrangement of hydration shell water molecules near a solute (yellow). The green atom denotes the center of the water molecule for which q parameter is calculated and the vertices are shown in red. The base of the tetrahedron (the central green particle and the nearby 3 red particles) are all in the first hydration shell of the solute.

**References:**


1. Jorgensen, W. L.; Maxwell, D. S.; Tirado-Rives, J. Development and Testing of the OPLS All-Atom Force Field on Conformational Energetics and Properties of Organic Liquids. *J. Am. Chem. Soc.* **1996**, *118*, 11225–11236.
2. Pial, T. S.; Das, S. Machine Learning Enabled Quantification of The Hydrogen Bonds Inside the Polyelectrolyte Brush Layer Probed Using All-Atom Molecular Dynamics Simulations. *Soft Matter* **2022**, *18*, 8945-8951.
3. Joung, I. S.; Cheatham, T. E. III. Determination of Alkali and Halide Monovalent Ion Parameters for Use in Explicitly Solvated Biomolecular Simulations. *J. Phys. Chem. B* **2008**, *112*, 9020–9041.
4. https://github.com/thatchristoph/vmd-cvs-github/blob/master/plugins/bossconvert/oplsaa.par
5. Veld, P.J. in't; Rutledge, G.C. Temperature-Dependent Elasticity of a Semicrystalline Interphase Composed of Freely Rotating Chains. *Macromolecules* **2003**, 36, 19, 7358–7365.
6. https://github.com/gromacs/gromacs/tree/main/share/top/oplsaa.ff
7. Sachar, H. S.; Sivasankar, V. S.; Das, S. Revisiting the Strong Stretching Theory for Ph-Responsive Polyelectrolyte Brushes: Effects of Consideration of Excluded Volume Interactions and An Expanded Form of The Mass Action Law. *Soft Matter* **2019**, *15*, 559-574.
8. Csajka, F. S.; Seidel, C. Strongly Charged Polyelectrolyte Brushes: A Molecular Dynamics Study. *Macromolecules* 2000, *33*, 2728-2739.

9. Biswas, A.; Priyadarshini, A.; Malik, B. S. Dynamics and Spectral Response of Water Molecules around Tetramethylammonium Cation. *J. Phys. Chem. B* **2019**, *123*, 8753–8766
10. Belch, A. C.; Berkowitz, M.; McCammon, J. A. Solvation Structure of a Sodium Chloride Ion Pair in Water. *J. Am. Chem. Soc.* **1986**, *108*, 1755-1761.
11. García-Tarrés, L.; Guàrdia, E. Hydration and Dynamics of a Tetramethylammonium Ion in Water: A Computer Simulation Study. *J. Phys. Chem. B* **1998**, *102*, 7448–7454
12. Duboué-Dijon, E.; Laage, D. Characterization of the Local Structure in Liquid Water by Various Order Parameters. *J. Phys. Chem. B* **2015**, *119*, 8406–8418.
13. Sachar, H. S.; Pial, T. H.; Desai, P. R.; Etha, S. A.; Wang, Y.; Chung, P. W.; Das, S. Densely Grafted Polyelectrolyte Brushes Trigger "Water-in-Salt"-like Scenarios and Ultraconfinement Effect. *Matter* **2020**, *2*, 1509–1521.
14. Zhang, X.; Laird, B. B.; Liang, H.; Lu, W.; Yu, Z.; Ma, X.; Cheng, Y.; Yang, Y. Atomistic characterization of the SiO2 high-density liquid/low-density liquid interface. *J. Chem. Phys.* **2022**, *157*, 1303.
15. Hande, V. R. and Chakrabarty, S. Structural Order of Water Molecules around Hydrophobic Solutes: Length-Scale Dependence and Solute–Solvent Coupling. *J. Phys. Chem. B* **2015**, *119*, 11346–11357.
16. Wu, X.; Lu, W.; Streacker, L. M.; Ashbaugh, H. S.; Amontz, D. B. Temperature-Dependent Hydrophobic Crossover Length Scale and Water Tetrahedral Order. *J. Phys. Chem. Lett.* **2018**, 9(5), 1012–1017
17. Chakrabarty, S.; Hande, V. Size-Dependent Order–Disorder Crossover in Hydrophobic Hydration: Comparison between Spherical Solutes and Linear Alcohols. *ACS Omega* **2022**, *7*(3), 2671–2678.

18. White, A.; Jiang, S. Local and Bulk Hydration of Zwitterionic Glycine and its Analogues through Molecular Simulations. *J. Phys. Chem. B* **2011**, *115*, 660–667.